



Bachelor Thesis

in Physics

Looking for very high energy gamma-ray emission
associated with PSR J1809-2332

Jonas Meyer

Supervisor: Dr. Alison Mitchell

Erlangen Centre for Astroparticle Physics

Submission date: 24-09-25

Abstract

This work aims to analyze gamma ray emission associated with PSR J1809-2332 with the H.E.S.S. telescope array. To achieve this data from all phases of H.E.S.S. is taken into account. First the spatial and spectral models of PSR J2809-2332 and the surrounding sources HESS J1800-240, HESS J1801-233, HGPSC 054, HGPSC 055 and V4641 Sgr are fitted. As the fit is limited due to the fixed positions of the sources, the highest ΔTS is reached for the Flascam dataset with 6.58 for the model of PSR J1809-2332. To improve the fit the data from multiple datasets is combined with reduced IRFs and freed positions. This way a ΔTS of 21.81 is reached. Furthermore H.E.S.S. 1 is investigated closer, as it showed a trend to more negative significances during the background estimation. Also a trend towards high tilt values is found, which can be likely be explained by the averaging of the IRFs over the whole phase and the degrading of the telescopes during the early stages of operation.

Contents

| | | |
|----------|---|-----------|
| 1 | Pulsar and Pulsar Wind Nebulae | 1 |
| 1.1 | Supernova Remnants | 1 |
| 1.2 | Pulsars | 1 |
| 1.3 | High energy gamma-rays | 2 |
| 1.3.1 | Leptonic mechanisms | 2 |
| 1.3.2 | Hadronic mechanisms | 2 |
| 1.4 | Air showers | 3 |
| 2 | Imaging Atmospheric Cherenkov Telescope (IACT) | 3 |
| 2.1 | High Energy Stereoscopic System (H.E.S.S.) | 4 |
| 2.1.1 | HGPS | 5 |
| 2.2 | Fermi- <i>LAT</i> | 5 |
| 3 | Analysis | 6 |
| 3.1 | Datasets | 6 |
| 3.2 | Analysis of the datasets seperatly | 6 |
| 3.3 | Further analysis of HESS 1 | 15 |
| 3.4 | Combined Dataset | 19 |
| 3.5 | Summary | 22 |
| A | Appendix A | 24 |
| | Bibliography | 35 |

1 Pulsar and Pulsar Wind Nebulae

1.1 Supernova Remnants

After a supernova the outer layers of the star are ejected and collide with the surrounding gas in the vicinity of the former star. This leads to shock fronts, as the ejected particles move faster than the speed of sound in the medium, where turbulent magnetic fields form (Angelis and Pimenta, 2018, p. 600). Over time the shock propagates outwards, while slowing down, which is a process of tens of thousands of years.

During the lifetime of the SNR, it enters multiple phases (Angelis and Pimenta, 2018, p.601). Directly after the explosion of the star the emitted gas can expand freely until it hits the surrounding gas. When this happens after about some hundred years, the collision of the two gases induces strong shock fronts, that are able to accelerate particles and produce x-ray emission. After further slowing down, a relatively thin shell is formed (less than 1 pc thick). In this shell the ionized hydrogen and oxygen recombine and radiative losses start to play a role, which slows down the gas even more. In the last phase the expansion of the gas is not supported by the inner core as the hot interior starts cooling. At this stage radio emission is observed.

As the SNR ages the magnetic fields confining the particles weaken. So the particles are accelerated over less time and thus have lower energies. In general the process of shock acceleration can result in the acceleration of protons to energies of hundreds of TeV.

1.2 Pulsars

A high mass star at the end of its lifetime in the main sequence has burned most of its hydrogen and cannot maintain its size against the gravitational pressure. The star starts to collapse, which leads to a temperature increase and the fusion of helium sets in. This process is continued multiple times, depending on the initial mass, until a massive iron core is formed, which has the highest binding energy. After this point a supernova can occur, which bursts away the outer layers of the star and leaves behind a neutron star or a black hole. Such a neutron star is stabilized by degenerated neutron gas and has strong magnetic fields as well as a high radial velocity (Angelis and Pimenta, 2018, p. 597 ff.), because both of these are preserved during the collapse but the radius of the star reduces. The magnetic fields induce strong electric fields, which lead to an acceleration of charged particles. These produce photons via pair production and synchrotron emission (see section 1.3.1). In combination with the radial velocity, this leads to a seemingly pulsed signal, if the magnetic field axis and the rotation axis are misaligned, which leads to the term pulsar for such stars. Pulsars and their surrounding gas clouds play an important role in the production of high energy gamma rays.

As the highly magnetized plasma, accelerated by the pulsar, streams outwards, it collides with the medium in the near vicinity of the pulsar. This leads to a significant speed reduction of the pulsar wind in the so called “termination shock” (Mitchell and Gelfand, 2022). At this shock front much of the energy, which is bound in the magnetic fields, is converted to particle energy, which leads to particle acceleration.

Directly after the Supernova explosion the Pulsar is surrounded only by low density plasma. This results in an initial phase of rapid expansion of the Pulsar Wind Nebula (PWN). As the expansion also leads to a decrease of the magnetic fields synchrotron emission decreases, while emission from the inverse compton effect (see section 1.3.1)

is increasing (Mitchell and Gelfand, 2022). When the expanding PWN hits the SNR it is decelerated and even pushed inwards, due to the differences in pressure between the PWN and the SNR. This “reverse shock” results in stronger magnetic fields, which increase the emission from synchrotron radiation again.

During the compression the pressure increases until it matches over even exceeds the one in the surrounding medium. From that point on the PWN is slowly accelerated again, which favors growth of Rayleigh-Taylor instabilities (Mitchell and Gelfand, 2022). As those disrupt the PWN high energy particles are emitted into the SNR.

The last stage in the evolution of the PWN is reached, when the pulsar is leaving the SNR due to its motion. At this point the pulsar moves supersonically and the high energy particles are ejected into the interstellar medium (Mitchell and Gelfand, 2022).

1.3 High energy gamma-rays

There are two main categories of mechanisms for the production of high energy gamma rays. One involves only leptonic interactions, and the other involves hadronic interactions.

1.3.1 Leptonic mechanisms

Since there are strong magnetic fields in neutron stars, charged particles are accelerated by the Lorentz force and radiate photons. This synchrotron radiation yields high energy gamma-rays, where the energy of those is proportional to the square of the acceleration (Demtröder, 2017, p.179f). As the particles are highly relativistic the emission of the photons is parallel to the velocity of the particle. Another way to end up with high energy gamma-rays is to take low energy photons from starlight or the cosmic microwave background and let them interact with high energy electrons. This process is called inverse Compton scattering, because as in Compton scattering an electron e^- and a photon γ scatter, but with the outcome that the electron $(e^-)^*$ transfers energy to the photon γ^* (Equation 1, Demtröder, 2016 p.80) .

$$e^- + \gamma \rightarrow (e^-)^* + \gamma^* \quad (1)$$

The combination of both of these effects leads to the synchrotron self-Compton mechanism (SSC). It is based on photons being emitted by ultrarelativistic electrons, which were accelerated by shocks. Then they gain energy via the inverse Compton scattering with their parent electrons (Angelis and Pimenta, 2018, p.586 ff.). The result are photon energies in a region of GeV to TeV (Figure 1).

1.3.2 Hadronic mechanisms

This mechanism is based on protons, which are accelerated by shocks and collide with the surrounding medium like molecular clouds. As the protons have higher energies than the mass of a pion, they produce pions of all charges. Of which the neutral pions π^0 decay into two gamma rays, with each gamma-ray holding roughly half the energy of the pion. With an energy of about 67.5 MeV the effect is visible in the spectral energy distribution and is part of the “pion bump” (Angelis and Pimenta, 2018, p.589 ff.). The other two pions π^+ and π^- result a muon and a muon neutrino, where the muon further decays into an electron, an electron neutrino and a muon neutrino.

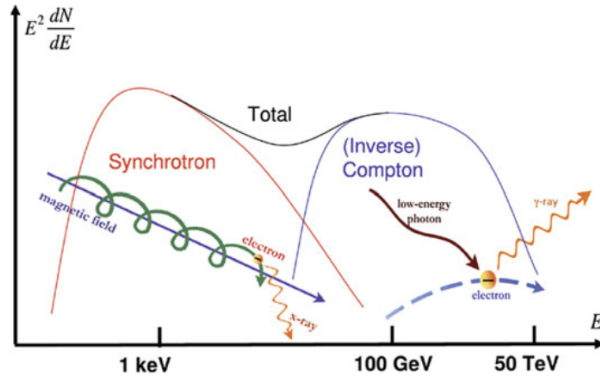


Figure 1: Energy spectrum for the combination of Synchrotron emission and inverse Compton scattering in the SSC, Angelis and Pimenta, 2018 p. 589

1.4 Air showers

When the high energy cosmic rays and photons from the acceleration mechanisms mentioned before hit Earth's atmosphere, they start a cascade of particle interactions. A photon produces an electron positron pair. Both of these particles still possess high enough energies to emit a photon via Bremsstrahlung, which can again produce an electron positron pair. As this process is repeated multiple times the number of particles rises quickly until the remaining energy of the emitted photons is not high enough to support further pair production (Angelis and Pimenta, 2018, p.124 ff.). Due to the cascading nature of the process it is called an air shower (Figure 2).

Protons also interact with the atmosphere but produce a hadronic air shower. Here mesons of all flavors are created. As already mentioned in section 1.3.2 the charged pions decay into a muon and a muon neutrino. And the muon further forms an electron, an electron neutrino and a muon neutrino. For the neutral pion the process is different than for charged pions, since it decays into two photons. These photons possess high enough energies to start an electromagnetic shower as described before.

In order to differentiate between electromagnetic and hadronic air showers, their spatial distribution is looked at. Air showers originated by a proton are more extended and vary in form more than ones started by a photon (Figure 2). This is because in hadronic cascades more different particles are involved and because of the larger transverse momentum for hadronic interactions.

2 Imaging Atmospheric Cherenkov Telescope (IACT)

The particles created in the air showers of the previous section move faster than the local speed of light, which results in the emission of Cherenkov light. This light is emitted as the molecules in the atmosphere relaxate after being polarised by the bypassing charged particle of the air shower. Since such a particle is highly relativistic the emitted photons are in phase and form a Cherenkov cone with an opening angle θ_c , which only depends on the refractive index of the atmosphere n and the speed of the particle v (Equation 2,

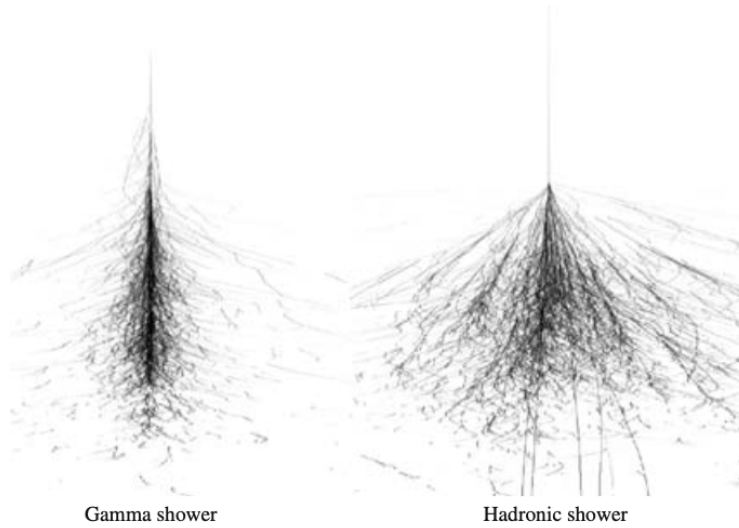


Figure 2: Comparison of electromagnetic (left) and hadronic (right) air showers; The hadronic shower is more broad and chaotic than the electromagnetic one. (Völk and Bernlöhr, 2009)

Angelis and Pimenta, 2018 p. 116 f.).

$$\cos(\theta_c) = \frac{c}{nv} \quad (2)$$

The cherenkov light is then collected by the mirrors of the Imaging Atmospheric Cherenkov Telescopes (IACTs) and captured onto a fast imaging camera (see Figure 3). When using multiple telescopes, the size and energy of the shower can be reconstructed with more significance. Also the arrival direction can be traced.

The advantage of the indirect detection of gamma rays on the ground is, that the effective detection area is determined as the area covered by Cherenkov light. This region is typically a circle with a diameter of 250 m and therefore much larger than that for satellites detecting gamma rays directly, which is typically below 1 m² (Actis et al., 2011). Therefore, higher energy gamma rays can be detected more easy despite their low flux. On the other hand the reconstruction of the initial properties of the gamma ray is more complicated. While the full extent can be determined easier, when the telescopes are further apart, it also makes it more unlikely for two telescopes to see the same air shower, when just the spacing between the telescope increases. As neutrinos from the decay of charged pions are not detected by Cherenkov Telescopes, the energy deposited in the neutrinos has to be taken into account for energy reconstruction (Angelis and Pimenta, 2018, p.128 f.).

2.1 High Energy Stereoscopic System (H.E.S.S.)

The H.E.S.S. telescope is operational since 2004 and is located in Namibia (Hinton and HESS Collaboration, 2004). It is an Imaging IACT Array, which originally consisted of 4 Telescopes, where this first configuration is referred to as Phase 1. As described before, it is advantageous to space the telescopes apart for better reconstruction, while



Figure 3: Image of the first two telescopes of H.E.S.S.; Hinton and HESS Collaboration, 2004

also keeping the area covered by the telescopes high. The compromise chosen for the H.E.S.S. is a square with a side of 120 m^2 , where the four telescopes (CT1 to CT4) are located at the corners (Hinton and HESS Collaboration, 2004).

In 2012 a fifth telescope, with a much larger diameter and a total light collection area of 600 m^2 , was inaugurated and marked the beginning of Phase 2. This new telescope brings a better angular and energy resolution, as well an increase in sensitivity at lower energies (H. E. S. S. Collaboration et al., 2018b).

A few years later in 2016 the cameras from the 4 telescopes of Phase 1 were replaced by newer electronics using the NECTAr chip in the now called Phase 1u. This was necessary because with CT5 the trigger rates went up and the dead time of the previous cameras could not keep up anymore. So the new cameras with reduced deadtime were installed.

In 2019, the camera of CT5 was also upgraded. This phase is referred to as Flashcam Era.

2.1.1 HGPS

The H.E.S.S. Galactic plane survey (HGPS) is a survey by the H.E.S.S. telescope of the region around the galactic plane in an energy between 0.1 and 100 TeV. Starting in 2004 until 2013 2700 hours of observations were combined to cover a region from 250° to 65° in longitude and a latitude between -3° and $+3^\circ$ (Figure 4, H. E. S. S. Collaboration et al., 2018a). Based on this data a catalog is created, which contains 78 VHE gamma-ray sources. As this catalog holds information about the position, the spectral model of the source as well as flux points, it is used as the reference value for the fit values in the analysis (see section 3.2).

2.2 Fermi-LAT

The Fermi satellite was launched on 11 June 2008 and holds two instruments. The first one is the gamma ray burst monitor and the second one is the Large Area Telescope. It detects gamma rays with energies from 20 MeV to 300 GeV (Atwood et al., 2009). As this instrument has a very large field of view, namely 20 % of the whole sky it can cover the sky in three hours (Atwood et al., 2009). Based on the observations of Fermi-LAT a

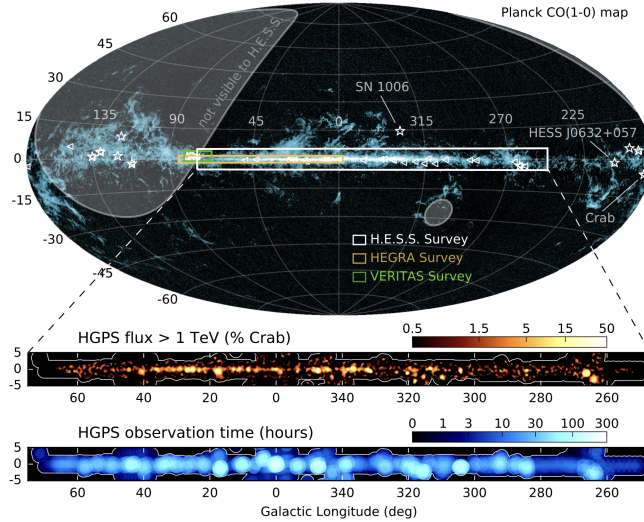


Figure 4: Region covered by the HGPS compared to HEGRA and VERITAS, H. E. S. S. Collaboration et al., 2018a

catalog is created. This work is using data from the fourth source catalog 4FGL, which was created with the first eight years of operation. It contains a total of 5064 sources measured with over 4σ significance (Abdollahi et al., 2020).

3 Analysis

3.1 Datasets

This work uses a total of 4 Datasets representing the four different phases of the H.E.S.S. Telescope. These will be referred to as the H.E.S.S. 1, H.E.S.S. 2, H.E.S.S. 1u and Flashcam datasets, with H.E.S.S. 1 being the largest dataset with a livetime of 52.20 h, followed by Flashcam with a comparable duration of 50.20 h. The other two datasets only have a livetime of 10.93 h (H.E.S.S. 1u) and 3.09 h (H.E.S.S. 2).

3.2 Analysis of the datasets separately

All the analysis has been done using `gammapy` Version 1.3. For further information and documentation see Donath et al., 2023 and Acero et al., 2025.

In this analysis the position of PSR J1809-2332 is defined as the center in the field of view (FoV), which has a width of 7 degrees in right ascension and a height of 6 degrees in declination. Other known sources in the FoV are added as masked region, where the size of the excluded regions is 1.2 times the extension of the gamma-ray emission as derived in previous analyses, to ensure that all emission is excluded (see Table 2 and Figure 5).

Based on this initial setup, the background is estimated for each run individually by fitting the spectral norm and tilt of the background model given for each run (Figure 6 and Figure 7).

For this background estimation also a safe energy threshold is defined with an energy bias

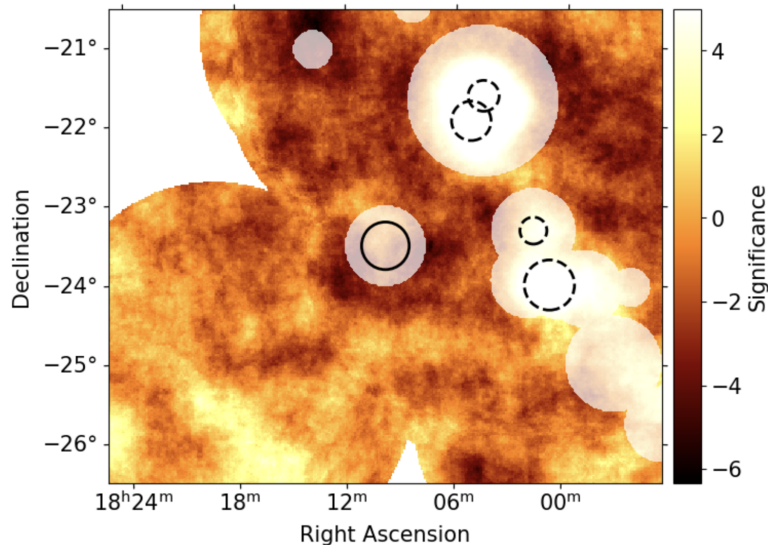


Figure 5: Significance map of the H.E.S.S. Phase 1 dataset where the dashed circles represent the location and extension of the surrounding sources listed in Table 3 and the full circle is centered around the position of PSR J1809-2332; the areas shown in white represent the exclusion regions

of 10%. This energy bias, which is calculated as the difference between reconstructed gamma energy and true gamma energy, is necessary, because a selection effect is happening towards the lower energy threshold. In order to avoid it the last energy bin with a bias below 10% is selected and the new save energy is chosen to be 10% above the highest energy in the bin (Aharonian et al., 2006). Together with the background peak, which is set as the bin after which the background spectrum peaks, the energy bias is used to set a safe energy threshold. The threshold is chosen to be at the higher energy of the two effects.

Already from the distribution of the tilt values in Figure 7, it can be seen that the H.E.S.S. 1 dataset is not centered around a tilt value of zero, as would be expected, but shifted toward higher tilt values. This is investigated in more detail in subsection 3.3. After that the runs are further processed by Gammapy’s ExcessMapEstimator, which computes the significance map per bin after Li & Ma (Equation 3 and Li and Ma, 1983).

$$S = \sqrt{2} \left(N_{on} \ln \left(\frac{1 + \alpha}{\alpha} \frac{N_{on}}{N_{on} + N_{off}} \right) + N_{off} \ln \left(\frac{1 + \alpha}{\alpha} \frac{N_{off}}{N_{on} + N_{off}} \right) \right)^{\frac{1}{2}} \quad (3)$$

In this process also the instrument response function (IRFs), which consist of the effective area, the point spread function and the energy dispersion matrix, are averaged over all runs and the data is combined into one dataset (Mohrmann et al., 2019).

The significance values from the significance maps (Figure 8) are taken pixel wise and plotted in a histogram. When restricting the histogram to all significance values outside of the exclusion regions, the result should be a normal distribution around a significance of 0, due to poisson statistics, if all emission has been excluded successfully.

This is the case for H.E.S.S. 2, H.E.S.S. 1u and Flashcam, however H.E.S.S. 1 shows a trend towards negative significances, which shifts the whole distribution to be centered

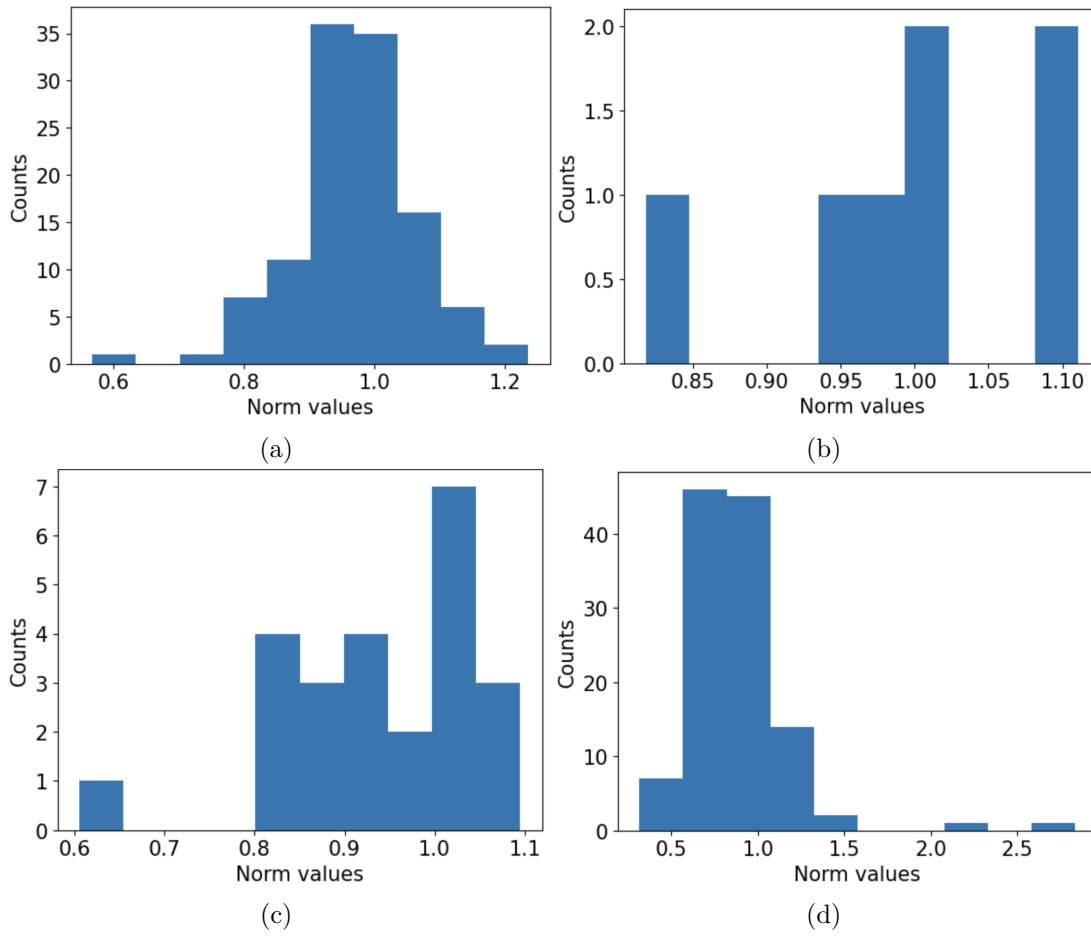


Figure 6: Histogram of the spectral norm distributions for (a) HESS 1, (b) HESS 2, (c) HESS 1u and (d) Flashcam; the expectation is a normal distribution centered around 1

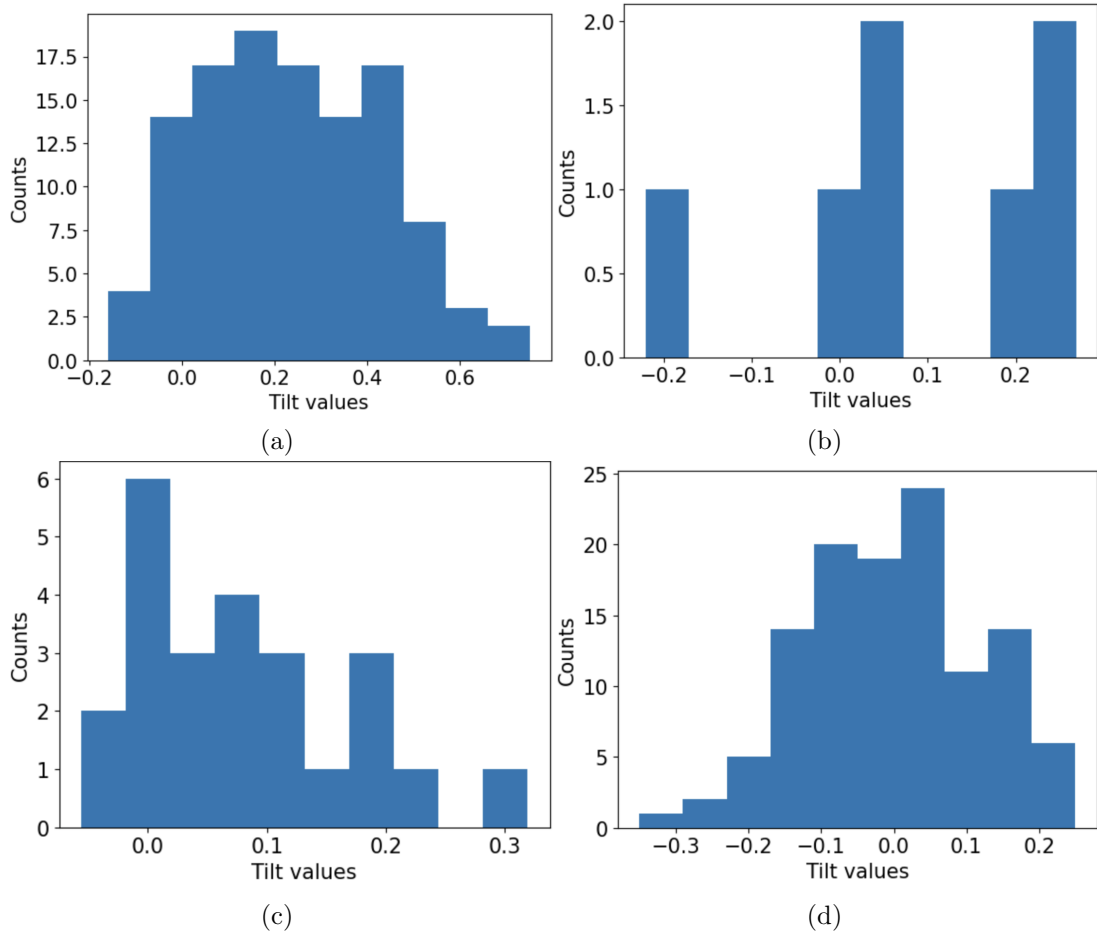


Figure 7: Histogram of the spectral tilt distributions for (a) HESS 1, (b) HESS 2, (c) HESS 1u and (d) Flashcam; the expectation is a normal distribution centered around 0; note the high offset of the tilt of HESS 1 towards high tilt values

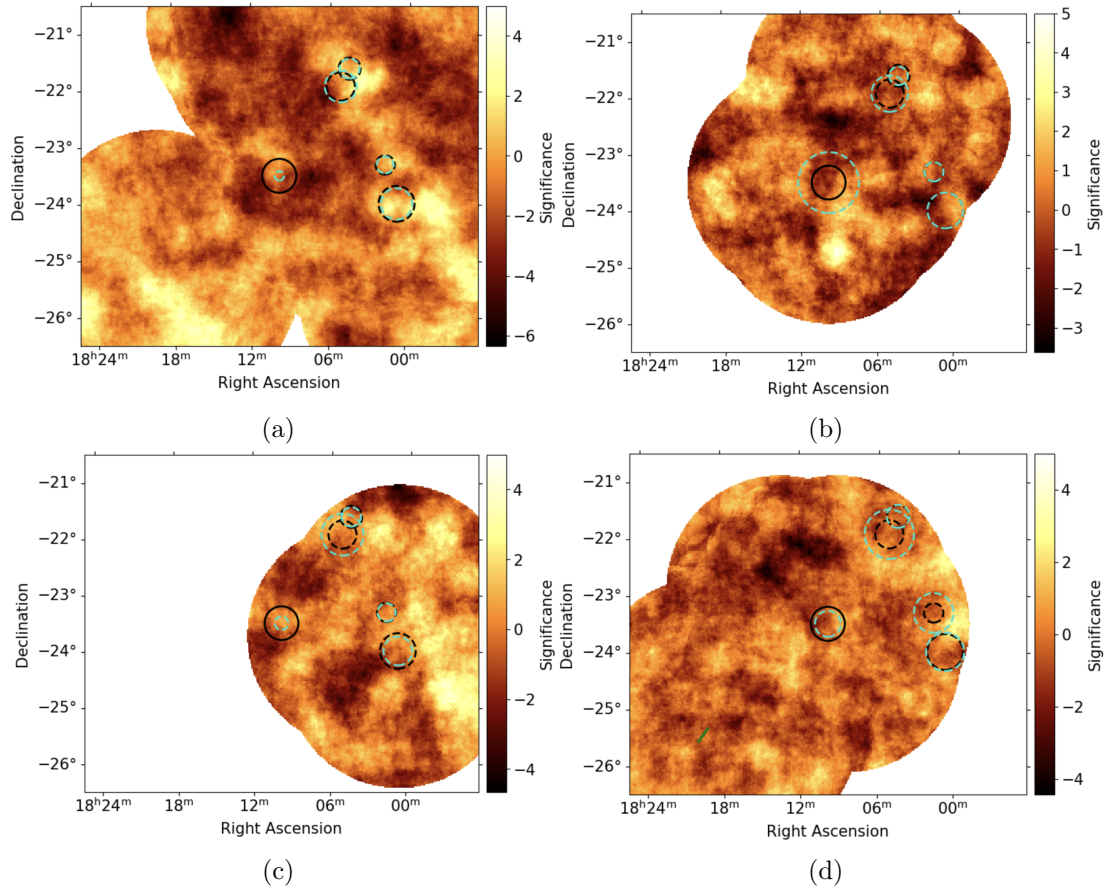


Figure 8: Significance map of all the datasets from H.E.S.S., where the black circles represent the location and extension of the surrounding sources listed in Table 3 and the green dashed circles the values after the fit ; (a) H.E.S.S. 1 , (b) H.E.S.S. 2, (c) H.E.S.S. 1u, (d) Flashcam: additionally the microquasar V4641 Sgr is added to the models (see. Table 3)

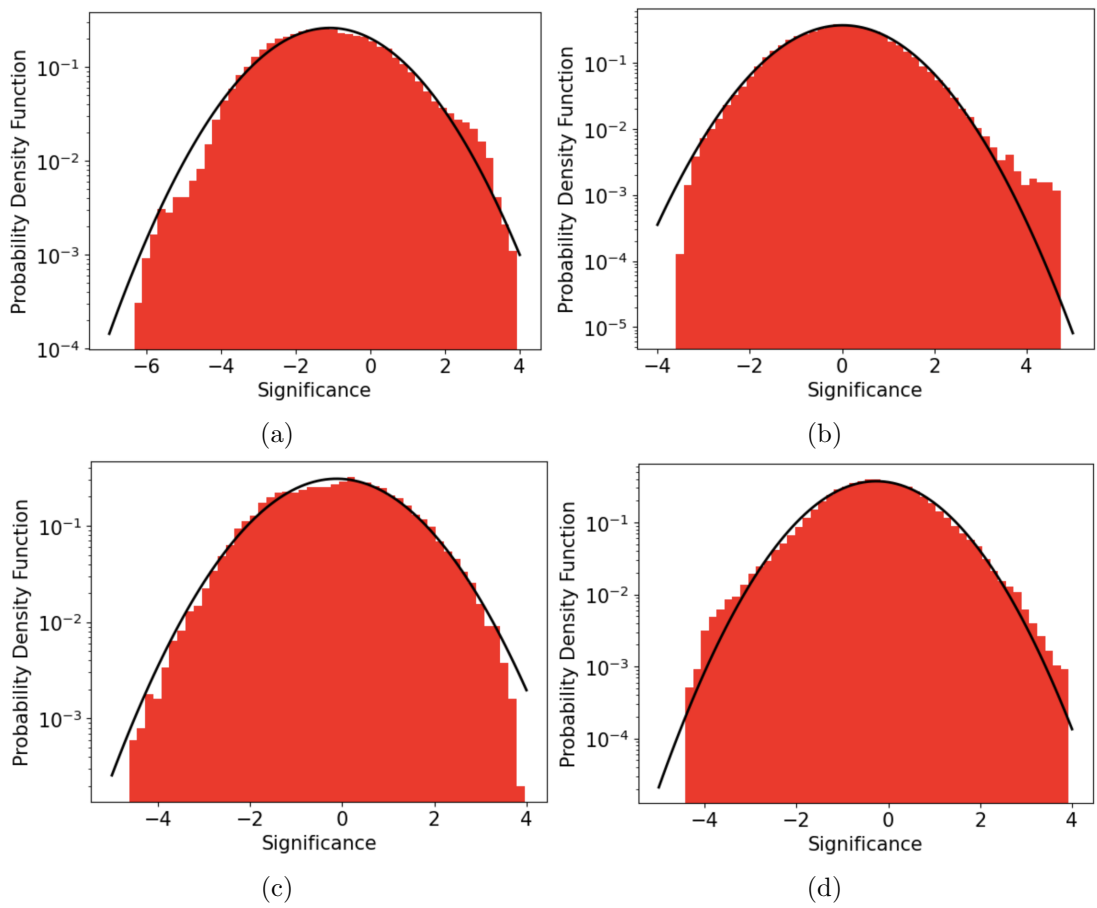


Figure 9: Significance histogram of (a) H.E.S.S. 1: Note the shift towards negative significances , (b) H.E.S.S. 2, (c) H.E.S.S. 1u, (d) Flashcam

around -1.09 (Figure 9). To determine whether this is caused by some single runs, the H.E.S.S. 1 data quality is further examined in subsection 3.3.

As already marked in Figure 8 the FoV used for this analysis contains three other known gamma-ray sources: HESS J1800-240, HESS J1801-233 and HESS J1804-216, where the last source consists of two components HGPSC 054 and HGPSC 055. Their location and extension can be found in Table 3 and are taken from the HGPS (H. E. S. S. Collaboration et al., 2018a). The parameters for V4641 Sgr are adopted from a currently ongoing study within the H.E.S.S. Collaboration.

HESS J1801-233 is associated with W 28 SNR and HESS J1800-240 is a molecular cloud illuminated by CRs accelerated at the SNR shock fronts. In the first analysis of HESS J1800-240 the source was divided in three components of which two are expected to be emission from CRs in nearby gas clouds (H. E. S. S. Collaboration et al., 2018a). However the H.E.S.S. cannot resolve these components in the HGPS.

During the analysis of the Flashcam Dataset, a gamma-ray signal was also detected from the microquasar V4641 Sgr (Figure 8 (d)). Therefore, this region is also excluded from the background estimation. The relevant parameters can be found in Table 3.

$$\Phi(\text{lon}, \text{lat}) = \frac{1}{2\pi\sigma} \exp\left(-\frac{1}{2} \frac{\theta^2}{\sigma^2}\right) \quad (4)$$

The sources mentioned before are modeled by a Gaussian spatial model (Equation 4, Acero et al., 2025) and a power law spectral model (Equation 5, Acero et al., 2025). The spatial models of HESS J1800-240, HESS J1801-233, HGPSC 054 and HGPSC 055 assume the sources to be symmetric. In contrast to that, V4641 Sgr shows a high ellipticity (0.985, Table 3).

$$\Phi(E) = \Phi_0 \left(\frac{E}{E_0}\right)^{-\Gamma} \quad (5)$$

Starting with the parameters in Table 3 the 4 (for the Flashcam dataset 5) nearby sources are fitted, with the longitude and latitude being fixed parameters. This is done because a single dataset cannot provide enough statistics to make the fit converge with freed positions. The fitting backend used here is “minuit” (Acero et al., 2025).

Another reason for the fit to diverge could be that the sources in all datasets apart from the HESS 1 dataset are located quite close to the edge of the field of view. In Figure 8 the results of the fit are visualized using the black dashed circles as the input values from the HGPS and the green dashed circle as the best-fit values derived in this study. In addition all parameters are listed in Table 4 to Table 7.

When looking at the total exposure of the datasets (Figure 10), the lower observation time for H.E.S.S. 1u and especially H.E.S.S. 2 is notable. The exposure maps also explain, why V4641 Sgr is only detected in with Flashcam, as this dataset is much more focused on the region around it. Also all datasets have in common that the exposure is never really centered around the location of HESS J1809-2332. The only exception is the H.E.S.S. 2 dataset, which has the shortest observation time.

Before comparing the fitted parameters to the values in the HGPS, it should be mentioned that in this analysis the spectral parameter and the position are fitted at the same time. However in the HGPS that is not the case and no 3d modelling was employed.

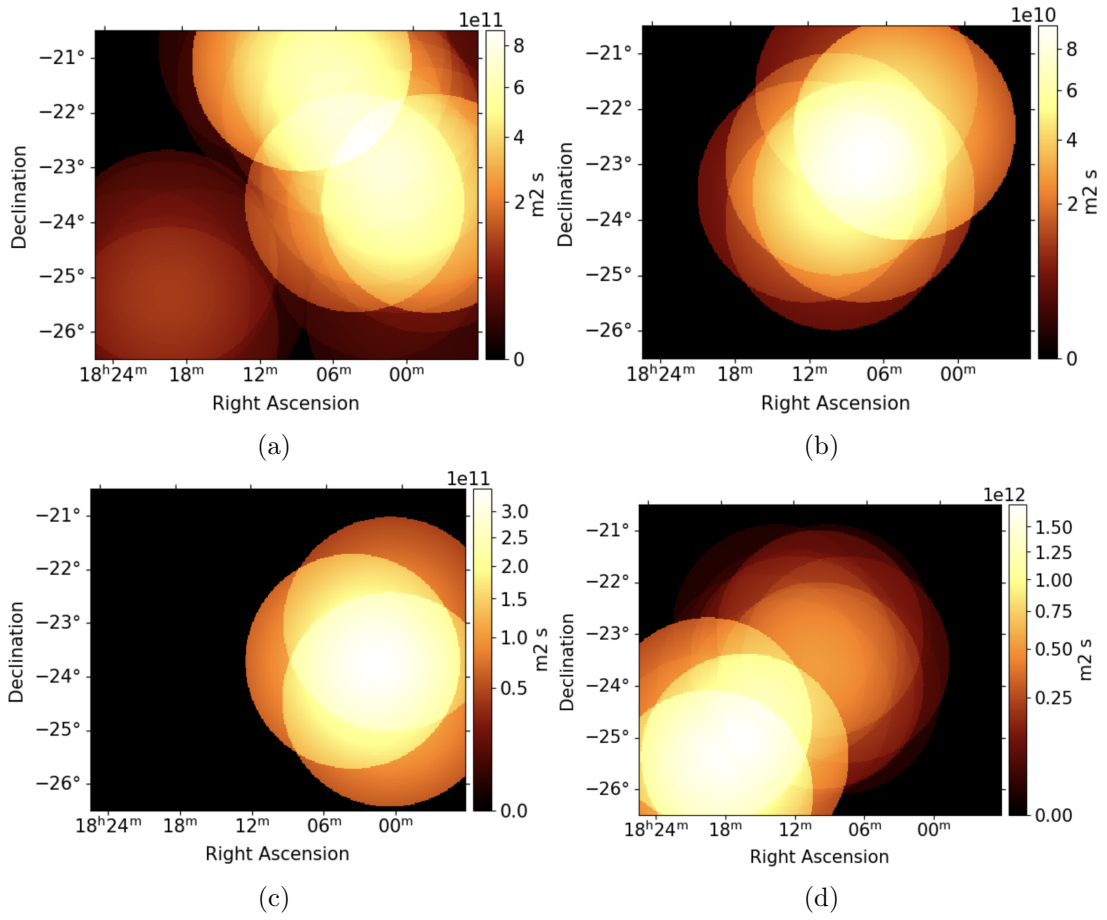


Figure 10: Map of the total exposure for (a) HESS 1, (b) HESS 2, (c) HESS 1u and (d) Flashcam

| | H.E.S.S. 1 | H.E.S.S. 2 | H.E.S.S. 1u | H.E.S.S. Flashcam |
|--|----------------------|----------------------|----------------------|----------------------|
| index | 1.828 ± 0.36 | 2.095 ± 0.50 | 2.288 ± 0.61 | 1.934 ± 0.23 |
| amplitude [$\frac{1}{\text{TeV s cm}^2}$] | $(1.29 \pm 1.1)e-13$ | $(1.58 \pm 1.5)e-12$ | $(3.14 \pm 3.1)e-13$ | $(4.19 \pm 2.7)e-13$ |
| reference [TeV] | 1.000 | 1.000 | 1.000 | 1.000 |
| longitude [deg] | 7.389 | 7.389 | 7.389 | 7.389 |
| latitude [deg] | -1.995 | -1.995 | -1.995 | -1.995 |
| sigma [deg] | 0.083 ± 0.04 | 0.540 ± 0.31 | 0.119 ± 0.06 | 0.229 ± 0.08 |
| e | - | - | - | - |
| phi [deg] | - | - | - | - |

Table 1: Fit values of PSR J1809-2332 for all datasets

As seen in Figure 8 the fitted spatial models for HESS J1800-240, HESS J1801-233, HGPS 054 and HGPS 055 agree with the HGPS values within errors for H.E.S.S. 1 and H.E.S.S. 2. For H.E.S.S. 1u HGPS 055 has a much greater extension with 0.373 ± 0.05 compared to the 0.249 ± 0.04 . Such an overestimation of HGPS 055 can also be observed for the flashcam dataset, where the extension is 0.435 ± 0.07 . In the same dataset also HESS J1801-233 is overestimated with 0.350 ± 0.08 compared to the 0.170 ± 0.03 .

The spectral models have two parameters that are fitted, the spectral index and the amplitude. For the index the fit values agree with those of the HGPS within errors, with the exception of HESS J1800-240 in the H.E.S.S. 1 dataset. There the index is 2.170 ± 0.07 compared to 2.473 ± 0.09 of the HGPS. Also the amplitude for this source is underestimated with $(3.49 \pm 0.43) \cdot 10^{-12} \frac{1}{\text{TeV s cm}^2}$ compared to $(4.80 \pm 0.41) \cdot 10^{-12} \frac{1}{\text{TeV s cm}^2}$. A similar underestimation of that source is observed for H.E.S.S. 1u. In the same dataset HGPS 054 and 055, which share one spectral model, show a significantly lower amplitude of $(1.14 \pm 0.13) \cdot 10^{-11} \frac{1}{\text{TeV s cm}^2}$ compared to $(2.13 \pm 0.062) \cdot 10^{-11} \frac{1}{\text{TeV s cm}^2}$. This trend is found in all other datasets as well. Only for HESS J1801-233 the source is overestimated with $(3.22 \pm 1.4) \cdot 10^{-12} \frac{1}{\text{TeV s cm}^2}$ compared to $(7.50 \pm 1.1) \cdot 10^{-13} \frac{1}{\text{TeV s cm}^2}$, which is due to the large extension of the source in the fit. The deviations in the spectral models compared to the HGPS can be explained by the simultaneous fit of morphology and spectral parameters employed in this work.

After this the parameters of all surrounding sources are frozen, and a model for PSR J1809-2332 is added to the list of models. Then a second fitting step is performed, which is also using “minuit” as the backend.

The results can be found in Table 1 and show large variation in the estimated extension of the source. H.E.S.S. 1 and H.E.S.S. 1u show a rather small extension with 0.083 ± 0.04 and 0.119 ± 0.06 , whereas Flashcam and H.E.S.S. 2 propose a much larger source with 0.229 ± 0.08 and 0.540 ± 0.031 . For the spectral index all fits agree within errors, but for the amplitude a comparison is not sensible as the error exceeds 64 % in every dataset. To check whether the proposed model of PSR J1809-2332 is statistically significant, a null-hypothesis test is performed. This allows a comparison of between two models, in this case the fitted values of PSR J1809-2332 and a null-hypothesis where the source is not present. The test statistic (TS) values of these models are used to calculate the TS difference and based on the ΔTS the significance is approximated.

For H.E.S.S. 1 ΔTS is 2.34, for H.E.S.S. 2 it is 1.56, for H.E.S.S. 1u 1.23 and for

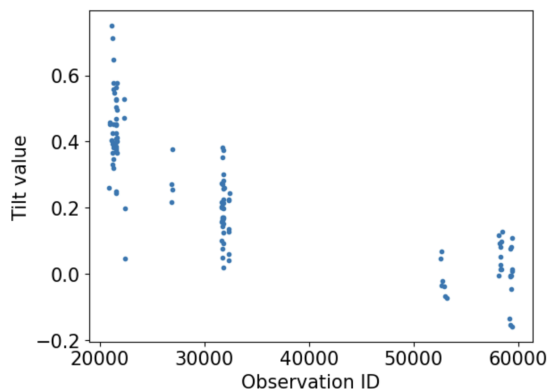


Figure 11: Plot of the Tilt values over the Observation ID for H.E.S.S. 1; note the trend to higher tilt values for earlier observation

flashcam 6.58.

Based on the analysis so far it can be stated, that none of the datasets alone can provide enough data at the location of PSR J1809-2332 to get a statistically significant model of the source. Overall the datasets need more observation time at the location of PSR J1809-2332, as this could help to model all the sources with freed positions, which currently limits the fit.

3.3 Further analysis of HESS 1

As the tilt of H.E.S.S. 1 show a shift towards higher tilt values, the tilt is checked for further trends in the data. All values are plotted over their Observation ID, which corresponds to the time the observation was taken.

For the first phase of H.E.S.S. the higher tilt values seem to be from earlier observations (below observation ID 25.000). Such a dependency can be explained by the degrading of the mirrors during the early stages of H.E.S.S.. Because all runs of the first phase use one averaged background model, the early runs have a higher efficiency and thus a higher tilt value.

Also the Zenith angle is plotted over the observation ID, as well as the tilt value over the zenith angle, to check for further trends in the data. But no correlation can be identified in Figure 12 for H.E.S.S. 1. For the other datasets no trends at all can be found (see Figure 21 to Figure 23).

As the histogram of the significance values for H.E.S.S. 1 showed more negative significances than expected, the background must be overestimated. In order to determine whether only a few runs are causing this problem, one looks at the tilt and norm for each run individually. This way runs, which overestimate the background can be identified (see Figure 13).

Another thing that could have happened is, that a certain energy bin is causing problems. To check for this the histogram of the significance is plotted again, but now for each energy bin of the 24 bins between 0.1 TeV and 100 TeV individually.

As the statistics for the lowest and highest energy bins are too low, to get sensible values for the peak μ and width σ of the significance distribution, they are excluded from the further analysis. In the early energy bins the fluctuations in the values for μ are larger

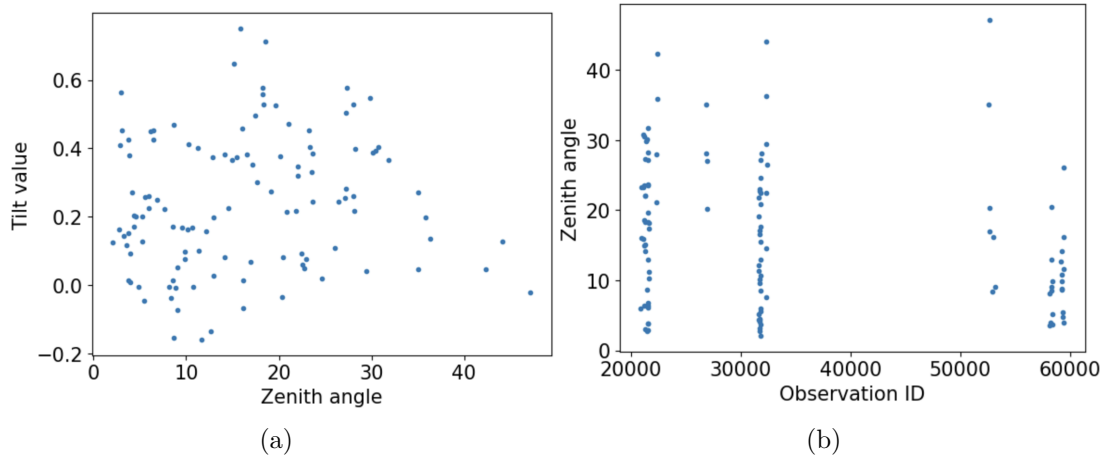


Figure 12: Plot of (a) Tilt over Zenith angle and (b) Zenith angle over observation ID for H.E.S.S. 1; no further trends are found

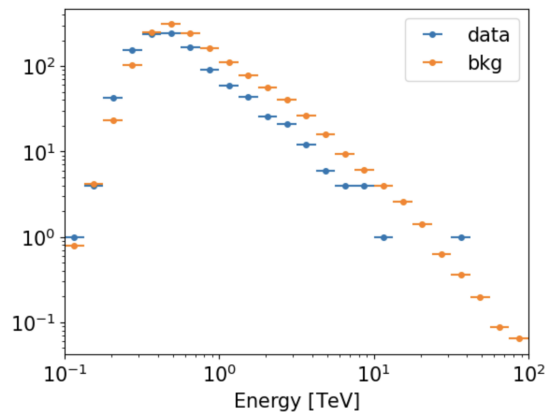


Figure 13: Run with Observation ID 22387 in H.E.S.S. 1, which shows a clear overestimation of the background

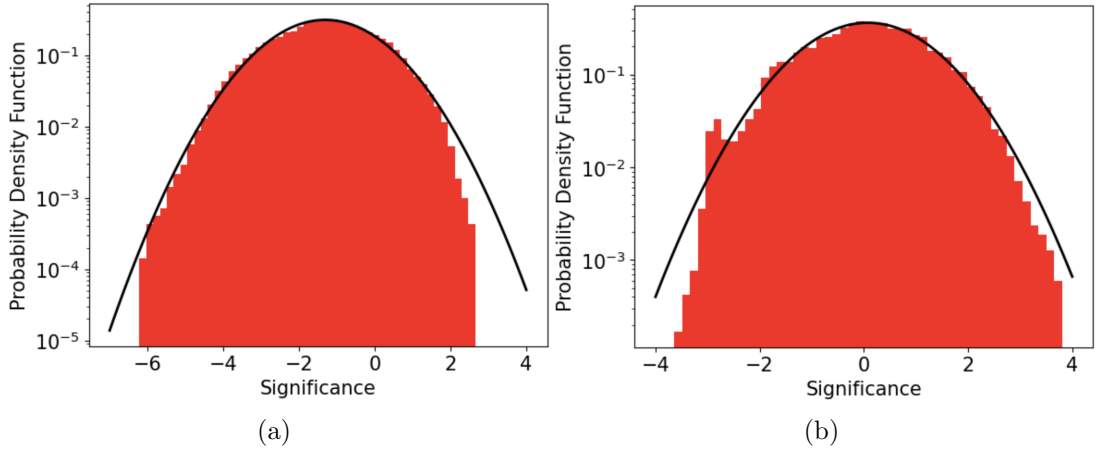


Figure 14: Plot of two significance histograms for (a) an early bin between 0.56 TeV and 0.75 TeV and (b) a later bin between 2.37 TeV and 3.16 TeV; the early bin shows a clear shift towards more negative significances, whereas the distribution for the later bin is centered around 0

due to the still lower statistics, but show a trend to more negative significances. This can be seen in Figure 14 for the energy bin between 0.56 TeV and 0.75 TeV. There μ has a value of -1.31 , while σ is 1.27. In later bins like the one between 2.37 TeV and 3.16 TeV, the significances are centered around 0 again. In this particular case μ is 0.08 and σ is 1.11.

Because the dataset shows a trend to higher tilt values for earlier runs, the dataset has been split into two subsets, one with observations below an ID of 25,000 and one with higher IDs. A possible reason for such an effect is that the instrument response functions are averaged over all runs of the first phase. This leads to a potential error for the first runs, due to the changes the telescope underwent during the early stages of operation. In this time the instrument and especially the mirrors degraded quickly, because of the sand and dust affecting the optical quality of the mirrors. That way early runs have a higher sensitivity, which is not accounted for in the averaged IRF and therefore potentially higher tilt values.

As seen in Figure 15 the early runs have higher tilt values with a peak at 0.47. Whereas the runs after Observation ID 25,000 are centered more around zero with a value of 0.1.

Also a thing to be checked are additional parameters during the observation, such as the muon efficiency for the telescopes CT1 to CT4, the trigger represented through the mean trigger rate (true rate mean), the slope of the trigger rate over the observation time (true rate delta1) and the difference between the trigger rate at the beginning and the end of the observation (true rate delta2), as well as the atmosphere with the mean transparency coefficient.

As it can be seen in Figure 16 and Figure 17 no trend is observed for the parameters. This means that there is no correlation between those parameters and the high tilt values in H.E.S.S. 1. For the telescopes CT2 to CT4 look similar and can be found in the appendix (Figure 24 to Figure 26).

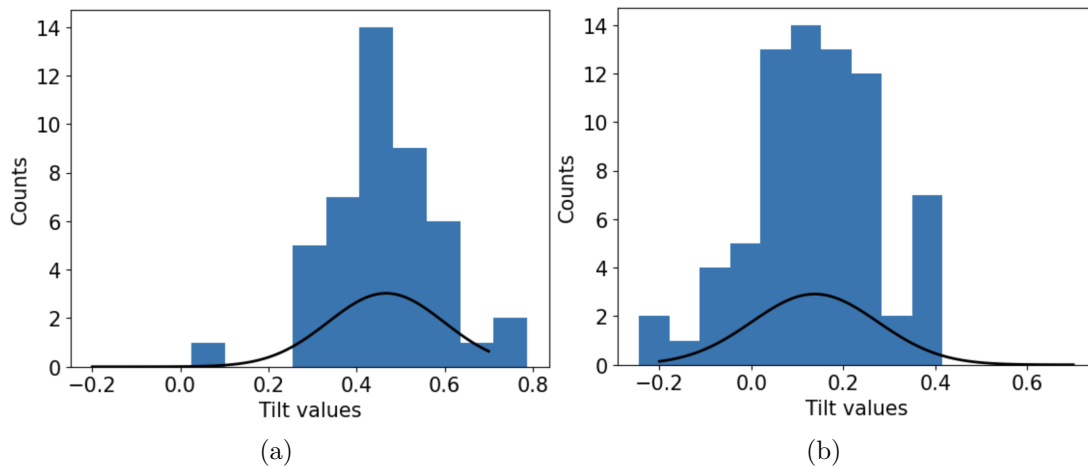


Figure 15: Plot of the tilt histograms for (a) all runs before Observation ID 25,000 of H.E.S.S. 1 and (b) all runs after Observation ID 25,000; the earlier runs show higher tilt values than later ones

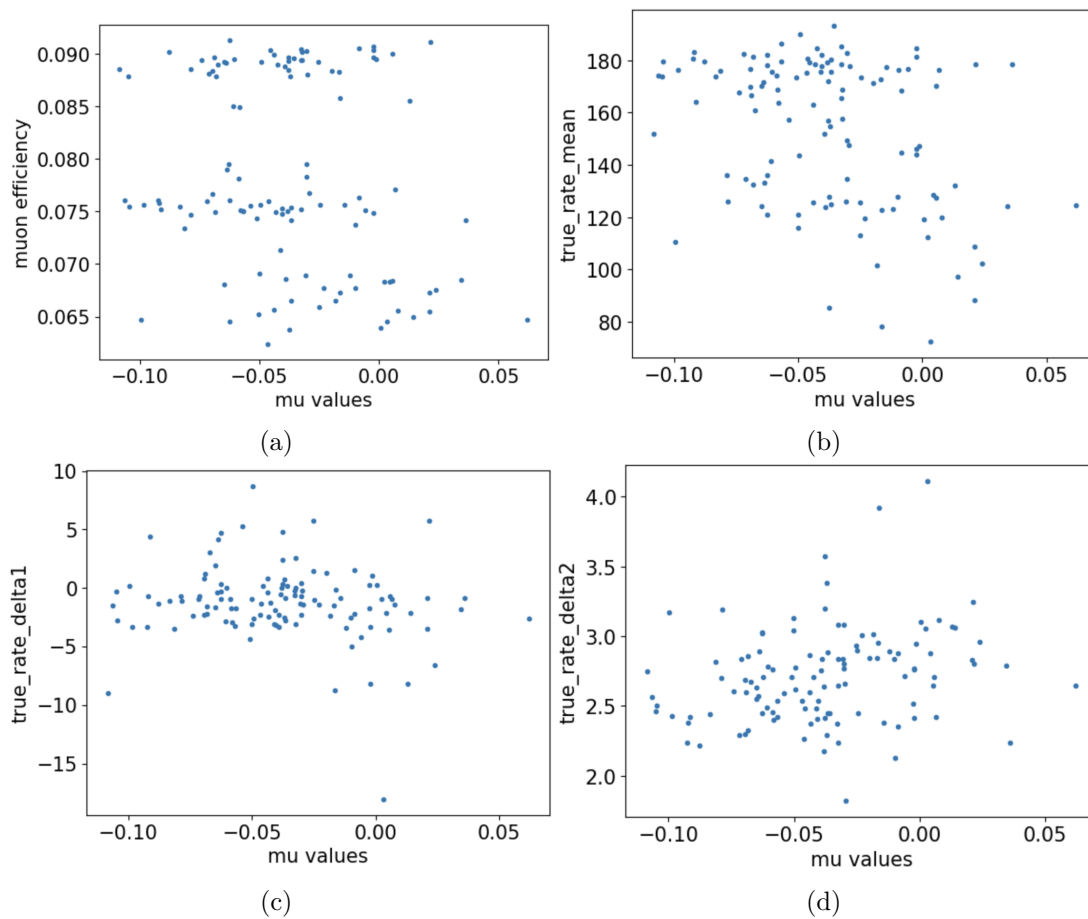


Figure 16: Check of additional parameters for CT1 (a) mean muon rate, (b) mean true rate, (c) true rate delta 1 (d) true rate delta 2

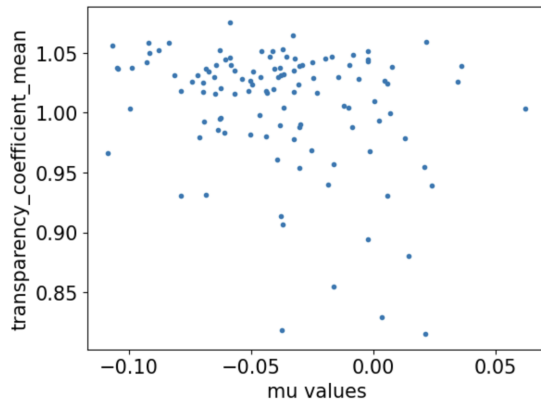


Figure 17: Mean transparency coefficient over mean significances of the runs from H.E.S.S. 1

3.4 Combined Dataset

Gammapy offers the possibility to also do the same analysis, as described in section 3.2, with all datasets at the same time. The difference to the analysis of a single dataset is, that the models are fit to all datasets at once. Since the IRFs of all used datasets need to be taken into account, H.E.S.S. 2 is excluded as it cannot provide enough data to justify one additional set of IRFs. Overall this method allows better statistics as much more data is used.

During the fitting process, which is carried out in two steps as described before, the positions of all sources can now be unfrozen.

The spatial model of HESS J1801-233 agrees within errors for the combined fit. Also the models of HGPSC 054 and 055 do agree with the data from HGPS, except for the latitude of the sources. With -0.018 ± 0.01 HGPSC 054 is slightly shifted compared to 0.004. A similar shift in latitude is observed for HGPSC 055, as well as for HESS J1800-240. For the last source also the longitude is shifted with 5.919 ± 0.03 compared to 5.959. Looking at the extension all sources mentioned before, with the exception of HGPSC 055, show a slightly smaller extension than in the HGPS, but still agree within errors.

In a comparison with the models in the single analysis of H.E.S.S. 1 the extensions have not changed much and agree with each other. Flashcam on the other side overestimated HESS J1801-233 and HGPSC 055, which both are now within errors for the combined fit.

For the spectral amplitudes the sources also agree with the HGPS, except for the shared model of HGPSC 054 and 055. There the amplitude is $(1.05 \pm 0.038) \cdot 10^{-11} \frac{1}{\text{TeV s cm}^2}$ compared to $(2.13 \pm 0.062) \cdot 10^{-11} \frac{1}{\text{TeV s cm}^2}$. And for the index only HESS J1800-240 shows a deviation with 2.251 ± 0.05 compared to 2.473 ± 0.09 .

For V4641 Sgr all spatial and spectral parameters agree within errors. And for PSR J1809-2332 again the null hypothesis test is run, to determine the statistic significance. The result is much more significant than all results for the single datasets with a ΔTS of 21.81 compared to 6.58 for Flashcam.

For the combined dataset also the spectral energy distribution (SED) for all sources are estimated. The Estimation is performed using Gammapy's FluxPointEstimator to

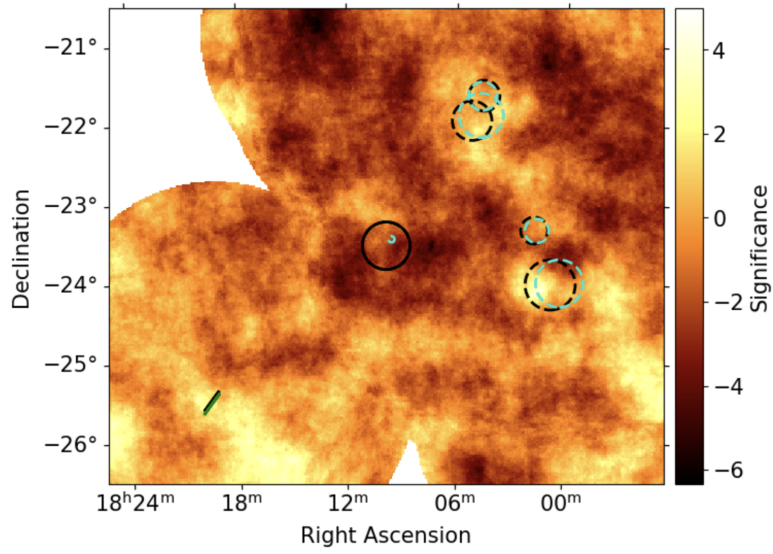


Figure 18: Fit values of the combined datasets visualized on the significance map of H.E.S.S. 1

evaluate six flux points for each source. For HESS J1800-240, HESS J1801-233 and HESS J1804-216 those are compared with the ones given in the HGPS (Figure 19). Flux points with a significance below 2σ are marked as upper limits.

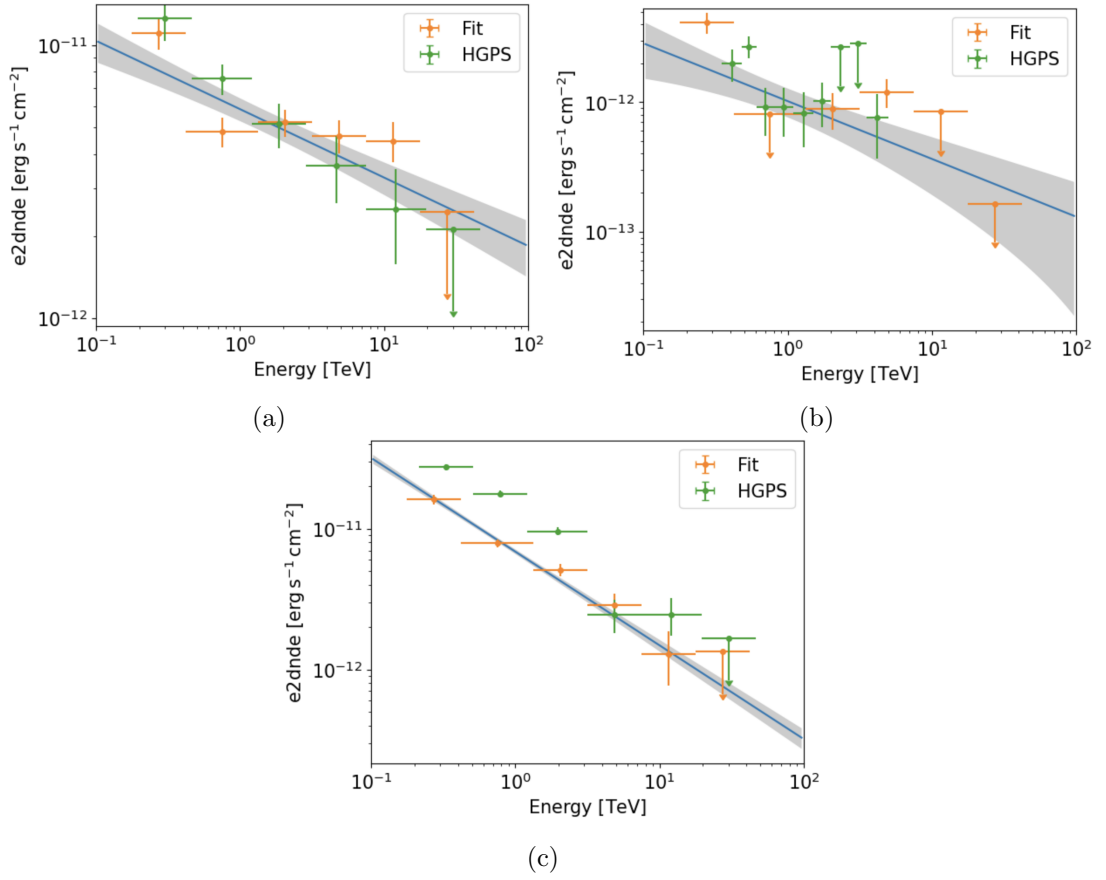


Figure 19: Flux points of (a) HESS J1800-240, (b) HESS J1801-233 and (c) HESS J1804-216, with a comparison to the flux points given in HGPS

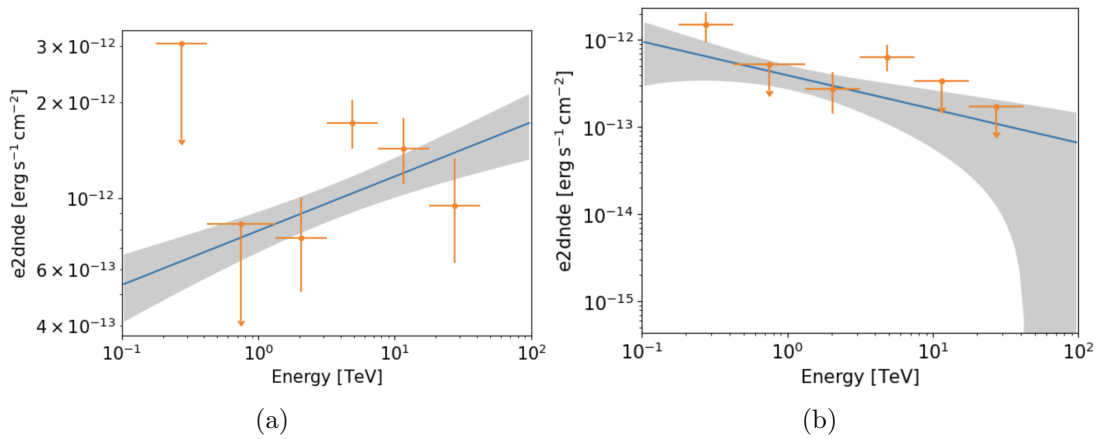


Figure 20: Flux points of (a) V4641 Sgr and (b) PSR J1809-2332 HGPS

3.5 Summary

In this work the spatial and spectral models of HESS J1800-240, HESS J1801-233, HGPSC 054, HGPSC 055, V4641 Sgr and PSR J1809-2332 were fitted. This was done for all phases of H.E.S.S.. As the datasets for each phase could not provide enough individual data to perform the fit with freed positions, all positions had to be frozen. Due to such a limitation the fits deviate when compared with HGPS, which is especially the case for the extension of HGPSC 055 in H.E.S.S. 1u and Flashcam with $(0.435 \pm 0.07)^\circ$ and $(0.350 \pm 0.08)^\circ$ compared to $(0.170 \pm 0.03)^\circ$. Also the spectral models show deviation, which can be explained by the simultaneous fit of morphology and spectral parameters employed here in contrast to the HGPS. Also for PSR J1809-2332 large variations in the extension are observed across the datasets. These are in a range between $(0.083 \pm 0.04)^\circ$ for H.E.S.S. 1 and $(0.540 \pm 0.31)^\circ$ for H.E.S.S. 2. Accordingly the significance values of the models of PSR J1809-2332 compared to the null hypothesis without this source is not very significant. The highest significance is reached for Flashcam with a ΔTS of 6.58, which corresponds to a σ of 2.57. H.E.S.S. 1 on the other side reaches only a ΔTS of 2.34, despite the fact that it has a similar lifetime as Flashcam. The reason for that is probably in the quality of the background estimation, since for H.E.S.S. 1 the significance distribution is not peaked around zero but at a significance of -1.09 (Figure 9 (a)). The further analysis of this dataset revealed a trend toward higher tilt values in the background estimation for earlier runs with an observation ID below 25,000 (Figure 11). Therefore the dataset was split in two subsets before and after observation ID 25,000 and the corresponding histograms of the tilt value (Figure 15) confirmed that trend. The reason for this is probably found in the IRFs, which are averaged over the whole phase. This way they don't take into account the higher sensitivity of the early runs, which degraded over time, which can lead to higher tilt values for those particular runs. Next to that the dataset was checked for further trends related to the zenith angle (Figure 12) of the observations or the atmospheric conditions represented by the mean transparency coefficient (Figure 17), but nothing was found. Also for several parameters of the trigger such as the true mean rate and delta 1 and 2 of the true rate, which were evaluated for each telescope individually, no correlations were detected (Figure 16). To increase the amount of data the previous datasets are combined and evaluated with reduced IRFs. Only H.E.S.S. 2 is excluded as the total livetime of 3.09 h is not enough to justify another set of IRFs. Due to the larger amount of data the positions of all 6 sources can now be unfrozen in the fit. The extensions of HESS J1800-240, HESS J1801-233, HGPSC 054 and HGPSC 055 agree within errors compared to HGPS, which was not the case for the fits of the single datasets. Also the model for PSR J1809-2332 shows a much larger significance with a ΔTS of 21.81 corresponding to a σ of 4.67. In the last step the SEDs of the sources were estimated as well and for HESS J1800-240, HESS J1801-233 and HESS J1804-216 compared to the values from HGPS (Figure 19).

Acronyms

H.E.S.S. High Energy Stereoscopic System.

HGPS H.E.S.S. Galactic plane survey.

IACT Imaging Atmospheric Cherenkov Telescope.

IRF Instrument Response Function.

PWN Pulsar Wind Nebula.

SNR Supernova Remnant.

A Appendix A

| Name | Longitude [deg] | Latitude [deg] | Radius [deg] |
|-----------------|-----------------|------------------------|--------------|
| HOTS J1754-257 | 3.730 | -0.009 | 0.4 |
| HOTS J1756-240 | 5.440 | 0.460 | 0.2 |
| HOTS J1757-245 | 4.700 | -0.190 | 0.5 |
| HESS J1800-240 | 5.960 | -0.380 | 0.2 |
| HESS J1800-240a | 6.141 | -0.629 | 0.39 |
| HESS J1800-240b | 5.902 | -0.365 | 0.33 |
| HESS J1800-240c | 5.711 | -0.059 | 0.4 |
| HESS J1801-233 | 6.657 | -0.268 | 0.44 |
| HESS J1804-216 | 8.401 | -0.033 | 0.79 |
| HOTS J1808-204 | 9.900 | -0.220 | 0.2 |
| HESS J1809-193 | 11.020 | $6.202 \cdot 10^{-14}$ | 0.7 |
| HOTS J1811-194 | 11.133 | -0.245 | 0.2 |
| HIP 88116 | 6.022 | -0.126 | 0.2 |
| HIP 89341 | 10.003 | -1.601 | 0.2 |

Table 2: List of the exclusion regions from the HGPS used for the background estimation

| | HESS J1800-240 | HESS J1801-233 | HGPS 054 | HGPS 055 | V4641 Sgr | PSR J1809-2332 |
|--|----------------------------------|---------------------------------|-----------------------------------|-----------------------------------|----------------------------------|-----------------------|
| index | 2.473 ± 0.09 | 2.660 ± 0.27 | 2.692 ± 0.04 | 2.692 ± 0.04 | 1.865 ± 0.09 | 2.000 |
| amplitude [$\frac{1}{\text{TeV s cm}^2}$] | $(4.80 \pm 0.41) \cdot 10^{-12}$ | $(7.50 \pm 1.1) \cdot 10^{-13}$ | $(2.13 \pm 0.062) \cdot 10^{-11}$ | $(2.13 \pm 0.062) \cdot 10^{-11}$ | $(1.32 \pm 0.25) \cdot 10^{-13}$ | $1.00 \cdot 10^{-13}$ |
| reference [TeV] | 0.954 | 1.000 | 0.716 | 0.716 | 2.000 | 1.000 |
| longitude [deg] | 5.959 | 6.657 | 8.449 | 8.248 | 6.731 | 7.389 |
| latitude [deg] | -0.442 | -0.268 | 0.004 | -0.285 | -4.866 | -1.995 |
| sigma [deg] | 0.316 ± 0.04 | 0.170 ± 0.03 | 0.195 ± 0.01 | 0.249 ± 0.04 | 0.319 ± 0.06 | 0.30 |
| e | - | - | - | - | 0.985 ± 0.01 | - |
| phi [deg] | - | - | - | - | 53.018 | - |

Table 3: Initial parameters of the surrounding sources; the first four sources are from the HGPS and V4641 Sgr is from an ongoing study within the H.E.S.S. collaboration

| | HESS J1800-240 | HESS J1801-233 | HGPSC 054 | HGPSC 055 |
|--|----------------------------------|---------------------------------|-----------------------------------|-----------------------------------|
| index | 2.170 ± 0.07 | 2.278 ± 0.26 | 2.679 ± 0.04 | 2.679 ± 0.04 |
| amplitude [$\frac{1}{\text{TeV s cm}^2}$] | $(3.49 \pm 0.43) \cdot 10^{-12}$ | $(5.06 \pm 1.6) \cdot 10^{-13}$ | $(1.09 \pm 0.039) \cdot 10^{-11}$ | $(1.09 \pm 0.039) \cdot 10^{-11}$ |
| reference [TeV] | 0.954 | 1.000 | 0.716 | 0.716 |
| longitude [deg] | 5.959 | 6.657 | 8.449 | 8.248 |
| latitude [deg] | -0.442 | -0.268 | 0.004 | -0.285 |
| sigma [deg] | 0.275 ± 0.03 | 0.148 ± 0.04 | 0.176 ± 0.01 | 0.281 ± 0.01 |
| e | - | - | - | - |
| phi [deg] | - | - | - | - |

Table 4: Fit values of the surrounding sources for the H.E.S.S. 1 dataset

| | HESS J1800-240 | HESS J1801-233 | HGPSC 054 | HGPSC 055 |
|--|----------------------------------|---------------------------------|----------------------------------|----------------------------------|
| index | 2.473 ± 0.09 | 2.660 ± 0.27 | 2.741 ± 0.21 | 2.741 ± 0.21 |
| amplitude [$\frac{1}{\text{TeV s cm}^2}$] | $(4.80 \pm 0.41) \cdot 10^{-12}$ | $(7.50 \pm 1.1) \cdot 10^{-13}$ | $(1.47 \pm 0.26) \cdot 10^{-11}$ | $(1.47 \pm 0.26) \cdot 10^{-11}$ |
| reference [TeV] | 0.954 | 1.000 | 0.716 | 0.716 |
| longitude [deg] | 5.959 | 6.657 | 8.449 | 8.248 |
| latitude [deg] | -0.442 | -0.268 | 0.004 | -0.285 |
| sigma [deg] | 0.316 ± 0.04 | 0.170 ± 0.03 | 0.164 ± 0.03 | 0.323 ± 0.07 |
| e | - | - | - | - |
| phi [deg] | - | - | - | - |

Table 5: Fit values of the surrounding sources for the H.E.S.S. 2 dataset

| | HESS J1800-240 | HESS J1801-233 | HGPSC 054 | HGPSC 055 |
|--|----------------------------------|---------------------------------|----------------------------------|----------------------------------|
| index | 2.380 ± 0.09 | 2.598 ± 0.24 | 2.595 ± 0.09 | 2.595 ± 0.09 |
| amplitude [$\frac{1}{\text{TeV s cm}^2}$] | $(3.49 \pm 0.52) \cdot 10^{-12}$ | $(9.16 \pm 2.7) \cdot 10^{-13}$ | $(1.14 \pm 0.13) \cdot 10^{-11}$ | $(1.14 \pm 0.13) \cdot 10^{-11}$ |
| reference [TeV] | 0.954 | 1.000 | 0.716 | 0.716 |
| longitude [deg] | 5.959 | 6.657 | 8.449 | 8.248 |
| latitude [deg] | -0.442 | -0.268 | 0.004 | -0.285 |
| sigma [deg] | 0.256 ± 0.03 | 0.160 ± 0.03 | 0.172 ± 0.02 | 0.373 ± 0.05 |
| e | - | - | - | - |
| phi [deg] | - | - | - | - |

Table 6: Fit values of the surrounding sources for the H.E.S.S. 1u dataset

| | HESS J1800-240 | HESS J1801-233 | HGPSC 054 | HGPSC 055 | V4641 Sgr |
|--|---------------------------------|---------------------------------|----------------------------------|----------------------------------|----------------------------------|
| index | 2.654 ± 0.31 | 2.426 ± 0.27 | 2.558 ± 0.13 | 2.558 ± 0.13 | 1.865 ± 0.09 |
| amplitude [$\frac{1}{\text{TeV s cm}^2}$] | $(5.23 \pm 2.0) \cdot 10^{-12}$ | $(3.22 \pm 1.4) \cdot 10^{-12}$ | $(1.25 \pm 0.22) \cdot 10^{-11}$ | $(1.25 \pm 0.22) \cdot 10^{-11}$ | $(1.32 \pm 0.25) \cdot 10^{-13}$ |
| reference [TeV] | 0.954 | 1.000 | 0.716 | 0.716 | 2.000 |
| longitude [deg] | 5.959 | 6.657 | 8.449 | 8.248 | 6.731 |
| latitude [deg] | -0.442 | -0.268 | 0.004 | -0.285 | -4.866 |
| sigma [deg] | 0.338 ± 0.07 | 0.350 ± 0.08 | 0.202 ± 0.03 | 0.435 ± 0.07 | 0.319 ± 0.06 |
| e | - | - | - | - | 0.985 ± 0.01 |
| phi [deg] | - | - | - | - | 53.018 |

Table 7: Fit values of the surrounding sources for the H.E.S.S. Flashcam dataset

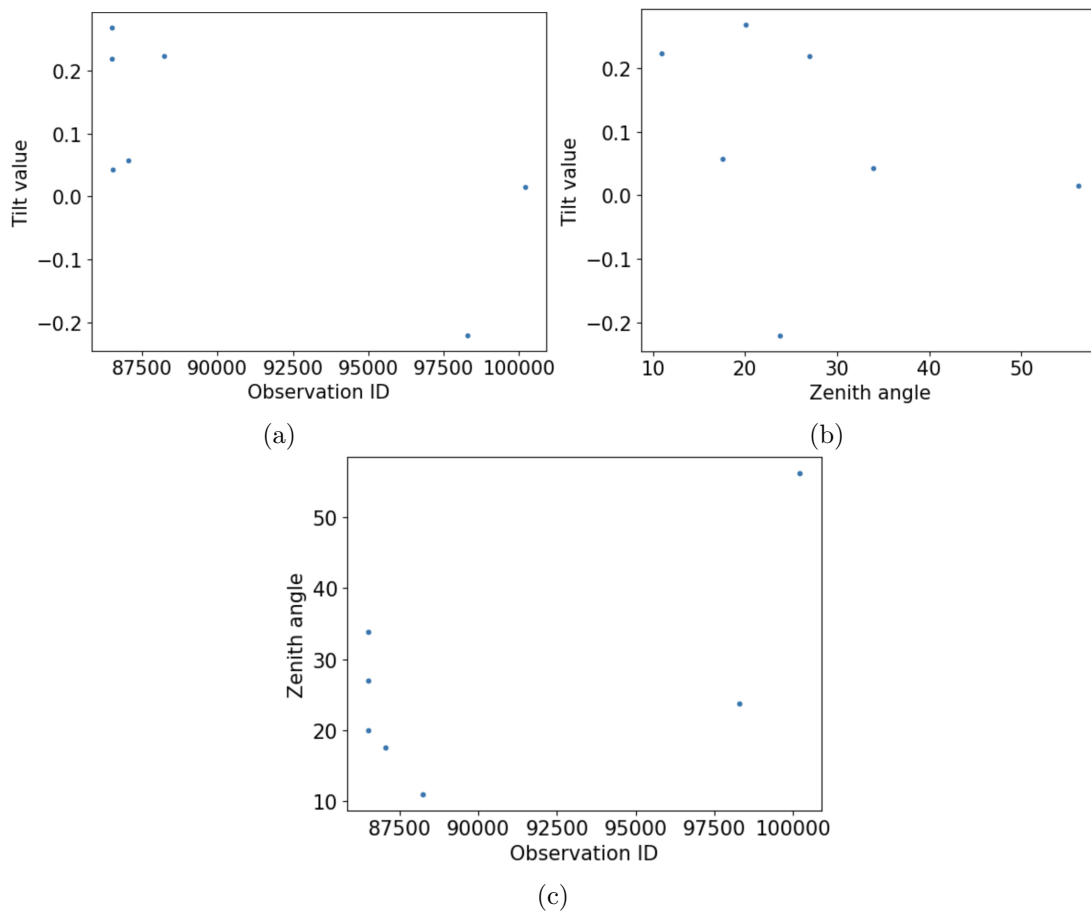


Figure 21: Plot of (a) Tilt over Observation ID, (b) Tilt over Zenith angle and (c) Zenith angle over observation ID for H.E.S.S. 2

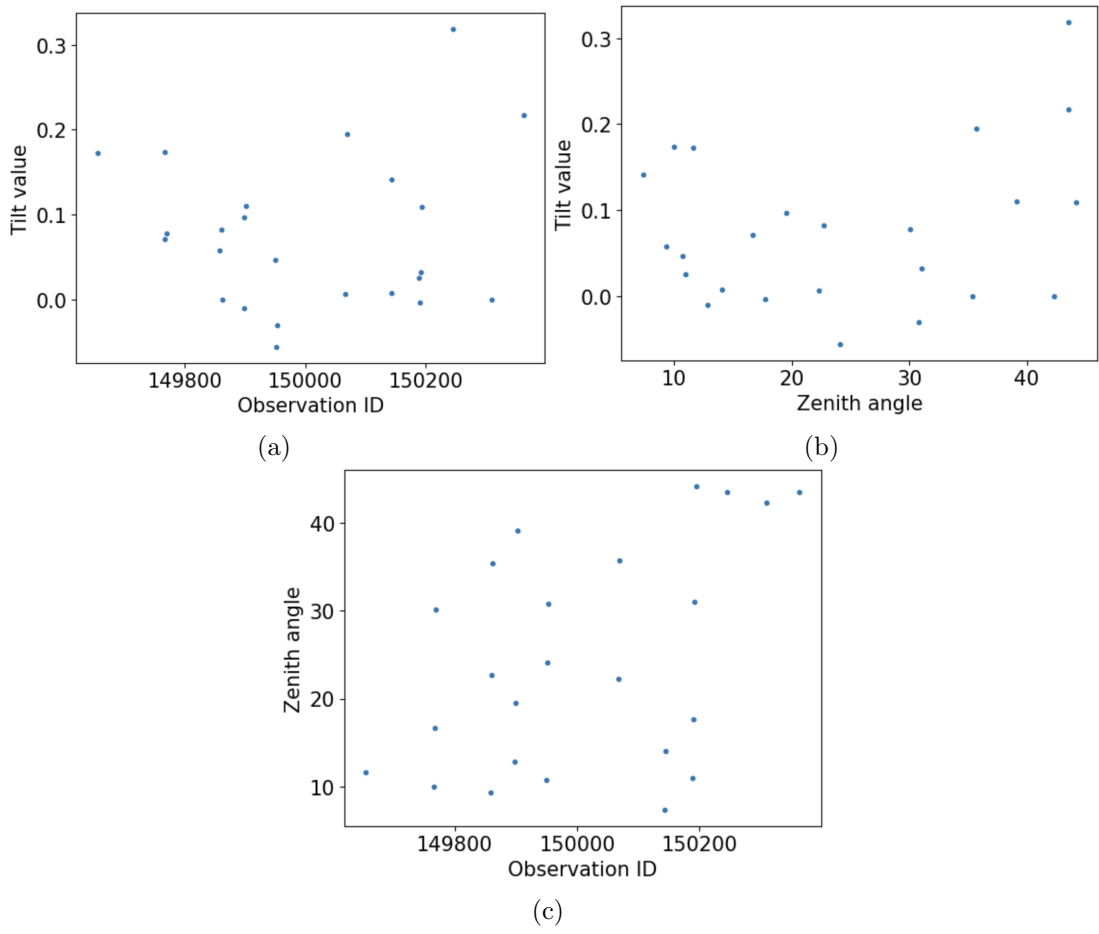


Figure 22: Plot of (a) Tilt over Observation ID, (b) Tilt over Zenith angle and (c) Zenith angle over observation ID for H.E.S.S. 1u

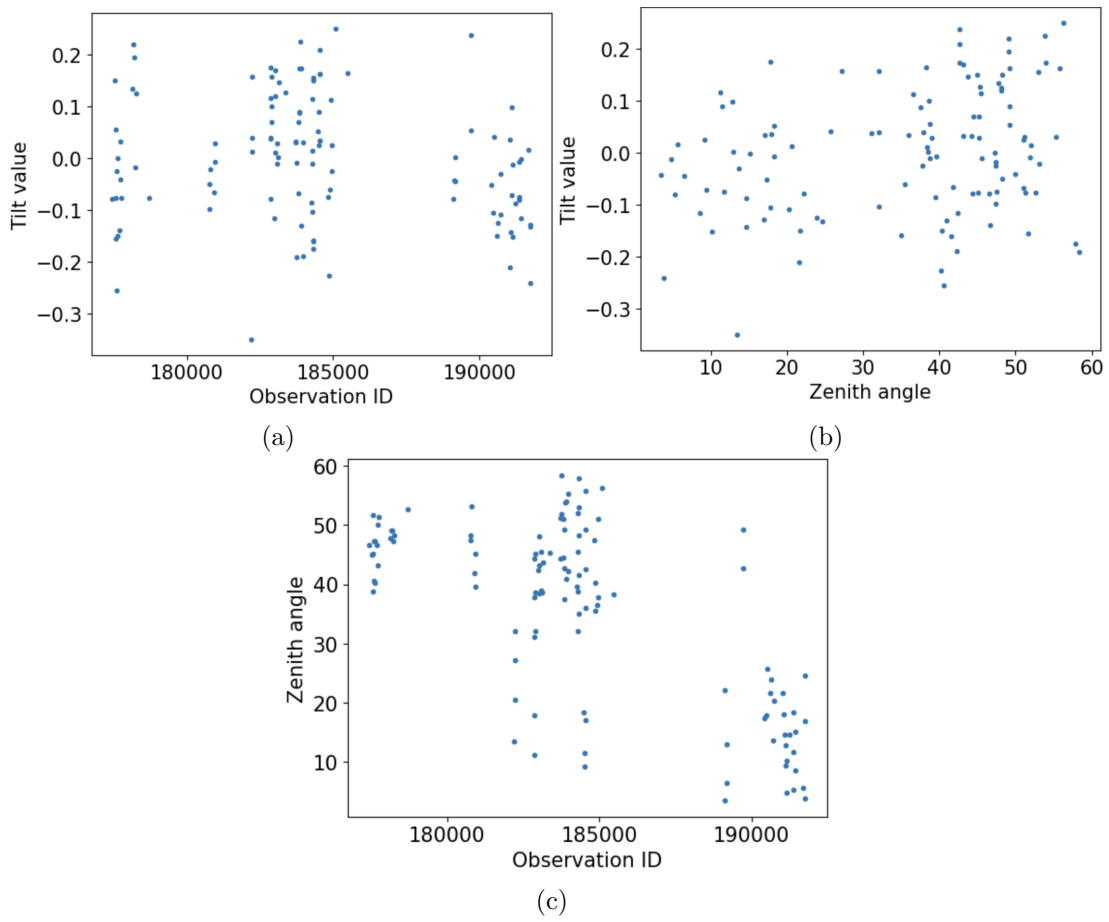


Figure 23: Plot of (a) Tilt over Observation ID, (b) Tilt over Zenith angle and (c) Zenith angle over observation ID for Flashcam

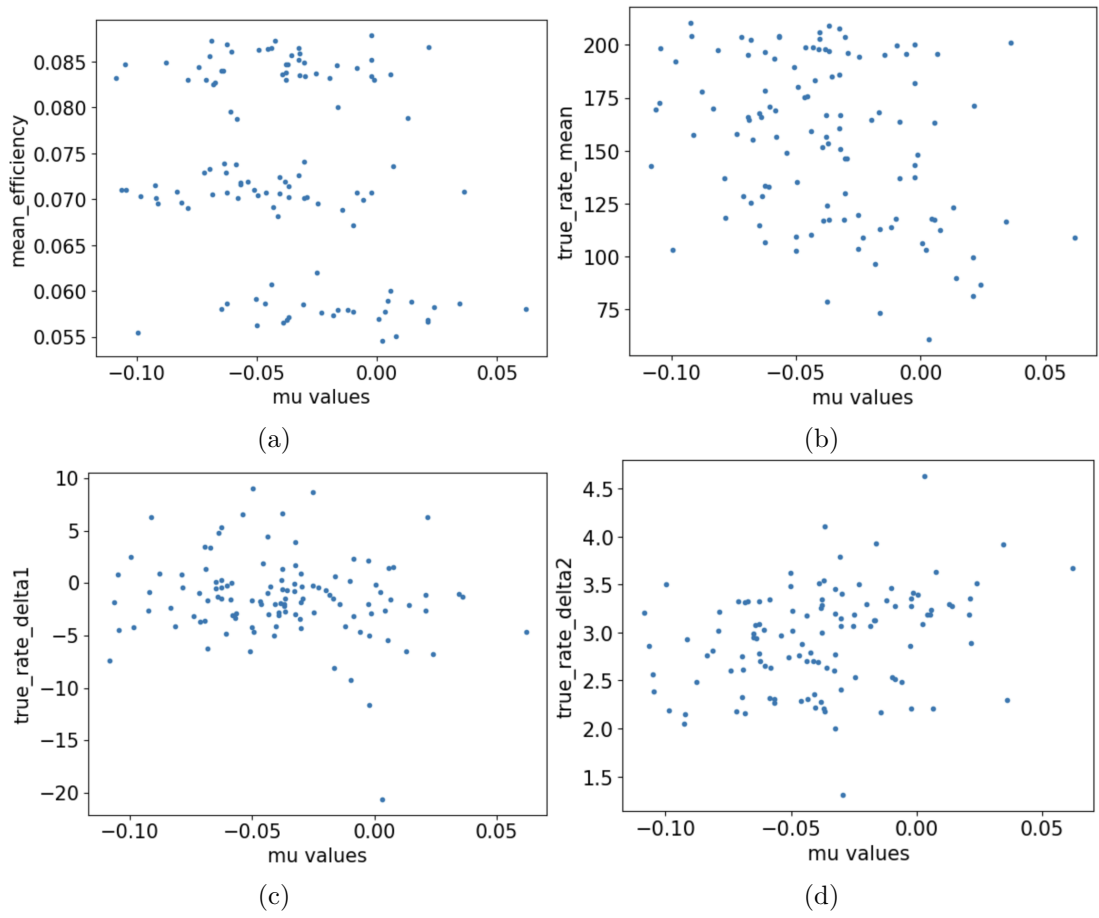


Figure 24: Check of additional parameters for CT2 (a) mean muon rate, (b) mean true rate, (c) true rate delta 1 (d) true rate delta 2

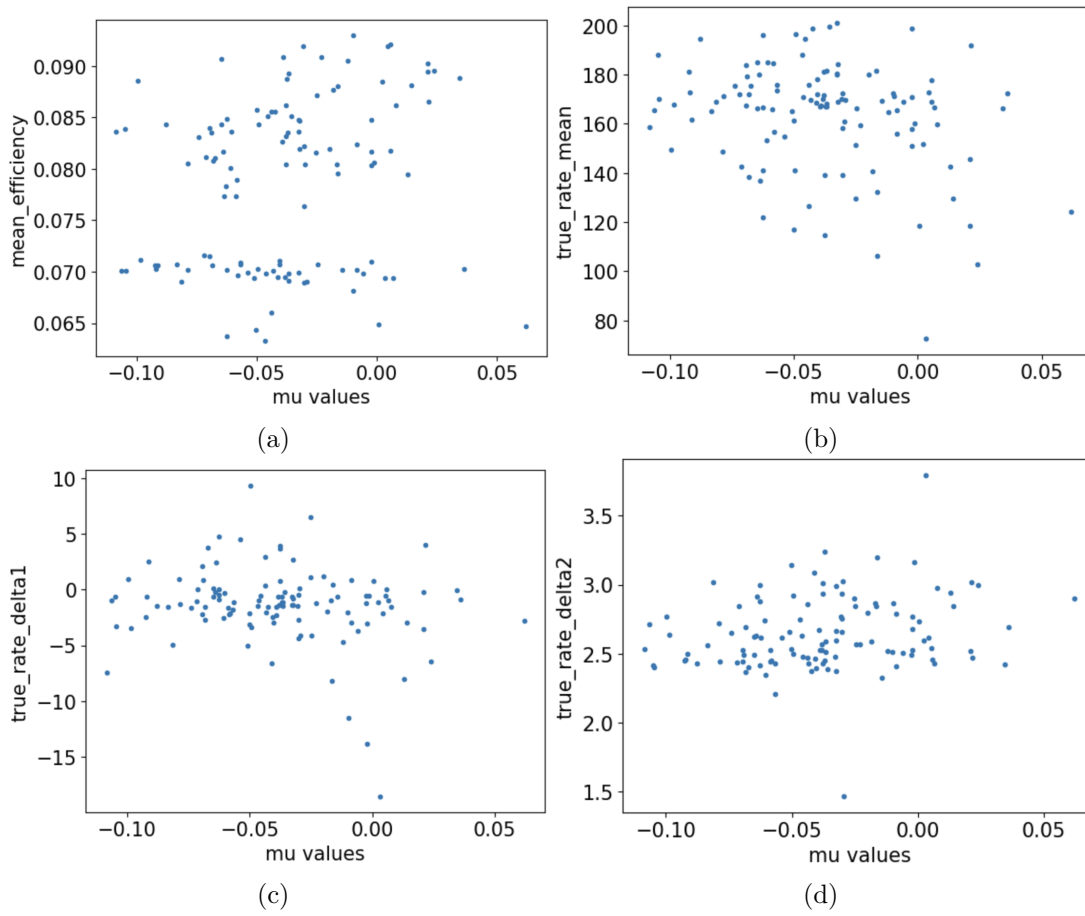


Figure 25: Check of additional parameters for CT3 (a) mean muon rate, (b) mean true rate, (c) true rate delta 1 (d) true rate delta 2

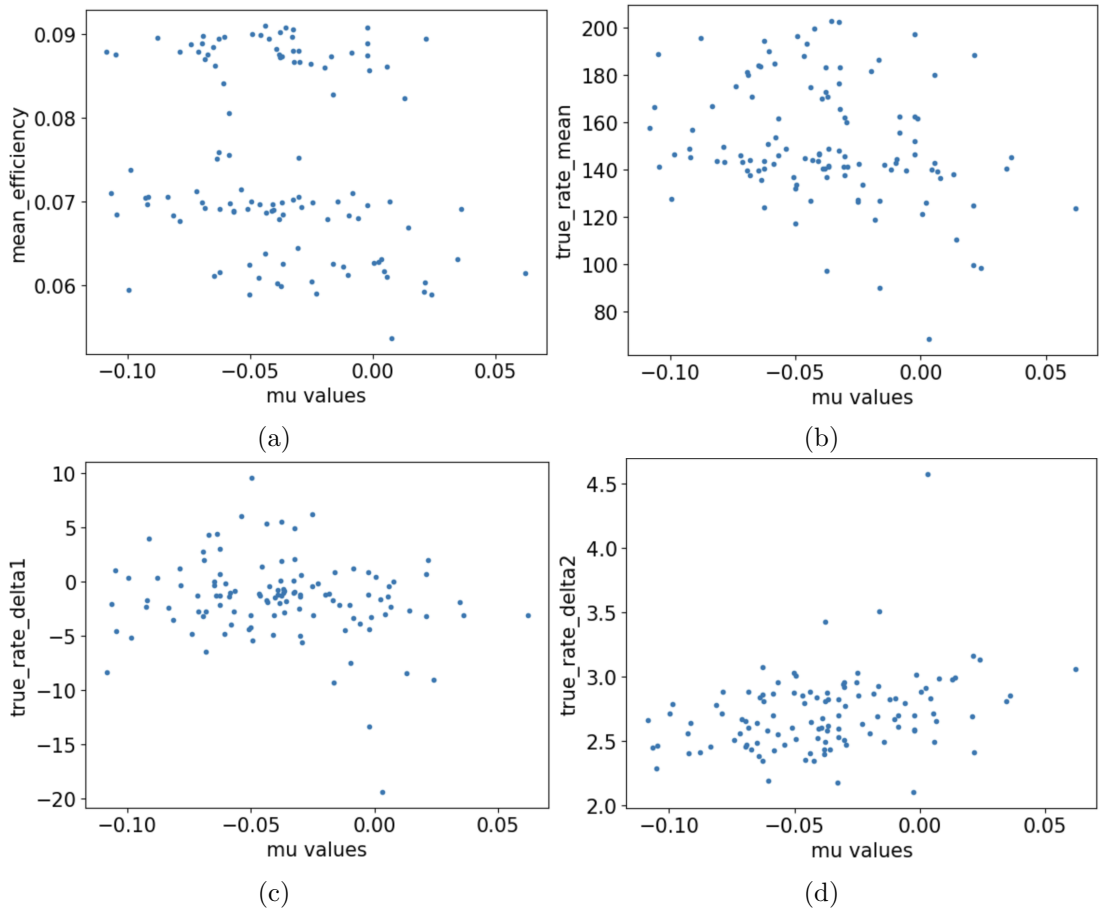


Figure 26: Check of additional parameters for CT4 (a) mean muon rate, (b) mean true rate, (c) true rate delta 1 (d) true rate delta 2

| | HESS J1800-240 | HESS J1801-233 | HGPSC 054 | HGPSC 055 | V4641 Sgr | PSR J1809-2332 |
|--|-----------------------------------|----------------------------------|------------------------------------|------------------------------------|-----------------------------------|-----------------------------------|
| index | 2.251 ± 0.05 | 2.447 ± 0.17 | 2.667 ± 0.03 | 2.667 ± 0.03 | 1.830 ± 0.06 | 2.388 ± 0.26 |
| amplitude | (4.05 ± 0.39) · 10 ⁻¹² | (6.37 ± 1.6) · 10 ⁻¹³ | (1.05 ± 0.038) · 10 ⁻¹¹ | (1.05 ± 0.038) · 10 ⁻¹¹ | (1.39 ± 0.18) · 10 ⁻¹³ | (2.45 ± 0.76) · 10 ⁻¹³ |
| $\left[\frac{1}{\text{TeV s cm}^2}\right]$ | 0.954 | 1.000 | 0.716 | 0.716 | 2.000 | 1.000 |
| reference [TeV] | 5.919 ± 0.03 | 6.636 ± 0.04 | 8.453 ± 0.02 | 8.251 ± 0.03 | 6.698 ± 0.04 | 7.429 ± 0.02 |
| longitude [deg] | -0.312 ± 0.03 | -0.241 ± 0.04 | -0.018 ± 0.01 | -0.153 ± 0.03 | -4.882 ± 0.03 | -1.897 ± 0.02 |
| latitude [deg] | 0.300 ± 0.02 | 0.151 ± 0.03 | 0.180 ± 0.01 | 0.280 ± 0.02 | 0.335 ± 0.01 | 0.038 ± 0.02 |
| sigma [deg] | - | - | - | - | 0.986 ± 0.00 | - |
| e | - | - | - | - | 53.018 | - |
| phi [deg] | - | - | - | - | - | - |

Table 8: Fit values of the combined fit for all sources; note that the positions of the sources are unfrozen now

Bibliography

- Abdollahi, S., F. Acero, M. Ackermann, M. Ajello, et al. (Mar. 2020). “Fermi Large Area Telescope Fourth Source Catalog”. In: 247.1, 33, p. 33. DOI: 10.3847/1538-4365/ab6bcb. arXiv: 1902.10045 [astro-ph.HE].
- Acero, Fabio, Arnau Aguasca-Cabot, Juan Bernete, Noah Biederbeck, et al. (Jan. 2025). *Gammapy v1.3: Python toolbox for gamma-ray astronomy*. Version v1.3. DOI: 10.5281/zenodo.14760974. URL: <https://doi.org/10.5281/zenodo.14760974>.
- Actis, M., G. Agnetta, F. Aharonian, A. Akhperjanian, et al. (Dec. 2011). “Design concepts for the Cherenkov Telescope Array CTA: an advanced facility for ground-based high-energy gamma-ray astronomy”. In: *Experimental Astronomy* 32.3, pp. 193–316. DOI: 10.1007/s10686-011-9247-0. arXiv: 1008.3703 [astro-ph.IM].
- Aharonian, F., A. G. Akhperjanian, A. R. Bazer-Bachi, M. Beilicke, et al. (Oct. 2006). “Observations of the Crab nebula with HESS”. In: 457.3, pp. 899–915. DOI: 10.1051/0004-6361:20065351. arXiv: astro-ph/0607333 [astro-ph].
- Angelis, Alessandro De and Mário Pimenta (2018). *Introduction to Particle and Astroparticle Physics*. Springer International Publishing AG.
- Atwood, W. B., A. A. Abdo, M. Ackermann, W. Althouse, et al. (June 2009). “The Large Area Telescope on the Fermi Gamma-Ray Space Telescope Mission”. In: 697.2, pp. 1071–1102. DOI: 10.1088/0004-637X/697/2/1071. arXiv: 0902.1089 [astro-ph.IM].
- Demtröder, Wolfgang (2016). *Experimentalphysik 3 Atome, Moleküle und Festkörper*. Springer Verlag.
- (2017). *Experimentalphysik 2 Elektrizität und Optik*. Springer Verlag.
- Donath, Axel, Régis Terrier, Quentin Remy, Atreyee Sinha, et al. (2023). “Gammapy: A Python package for gamma-ray astronomy”. In: *AA* 678, A157. DOI: 10.1051/0004-6361/202346488. URL: <https://doi.org/10.1051/0004-6361/202346488>.
- H. E. S. S. Collaboration, H. Abdalla, A. Abramowski, F. Aharonian, et al. (Apr. 2018a). “The H.E.S.S. Galactic plane survey”. In: 612, A1, A1. DOI: 10.1051/0004-6361/201732098. arXiv: 1804.02432 [astro-ph.HE].
- H. E. S. S. Collaboration, H. Abdalla, F. Aharonian, F. Ait Benkhali, et al. (Dec. 2018b). “First ground-based measurement of sub-20 GeV to 100 GeV γ -Rays from the Vela pulsar with H.E.S.S. II”. In: 620, A66, A66. DOI: 10.1051/0004-6361/201732153. arXiv: 1807.01302 [astro-ph.HE].
- Hinton, J. A. and HESS Collaboration (Apr. 2004). “The status of the HESS project”. In: 48.5-6, pp. 331–337. DOI: 10.1016/j.newar.2003.12.004. arXiv: astro-ph/0403052 [astro-ph].
- Li, T. P. and Y. Q. Ma (Sept. 1983). “Analysis methods for results in gamma-ray astronomy.” In: 272, pp. 317–324. DOI: 10.1086/161295.

- Mitchell, A. M. W. and J. Gelfand (2022). “Pulsar Wind Nebulae”. In: *Handbook of X-ray and Gamma-ray Astrophysics*. Ed. by Cosimo Bambi and Andrea Sanganelo, 61, p. 61. DOI: 10.1007/978-981-16-4544-0_157-1.
- Mohrmann, L., A. Specovius, D. Tiziani, S. Funk, et al. (Dec. 2019). “Validation of open-source science tools and background model construction in γ -ray astronomy”. In: 632, A72, A72. DOI: 10.1051/0004-6361/201936452. arXiv: 1910.08088 [astro-ph.IM].
- Völk, Heinrich J. and Konrad Bernlöhr (2009). “Imaging very high energy gamma-ray telescopes”. In: *Experimental Astronomy*. DOI: 10.1007/s10686-009-9151-z.

Acknowledgements

- This work made use of Gammapy (Donath et al., 2023), a community-developed Python package. The Gammapy team acknowledges all Gammapy past and current contributors, as well as all contributors of the main Gammapy dependency libraries: NumPy, SciPy, Astropy, Astropy Regions, iminuit, Matplotlib.
- This work uses the automatic spell and grammar check of Overleaf

Declaration of Originality

I, Jonas Meyer, student registration number: 23134760, hereby confirm that I completed the submitted work independently and without the unauthorized assistance of third parties and without the use of undisclosed and, in particular, unauthorized aids. This work has not been previously submitted in its current form or in a similar form to any other examination authorities and has not been accepted as part of an examination by any other examination authority.

Where the wording has been taken from other people's work or ideas, this has been properly acknowledged and referenced. This also applies to drawings, sketches, diagrams and sources from the Internet.

In particular, I am aware that the use of artificial intelligence is forbidden unless its use as an aid has been expressly permitted by the examiner. This applies in particular to chatbots (especially ChatGPT) and such programs in general that can complete the tasks of the examination or parts thereof on my behalf.

Any infringements of the above rules constitute fraud or attempted fraud and shall lead to the examination being graded "fail" ("nicht bestanden").

Place, Date

Signature